

Four-Carbon Criegee Intermediate from Isoprene Ozonolysis: Methyl Vinyl Ketone Oxide Synthesis, Infrared Spectrum, and OH Production

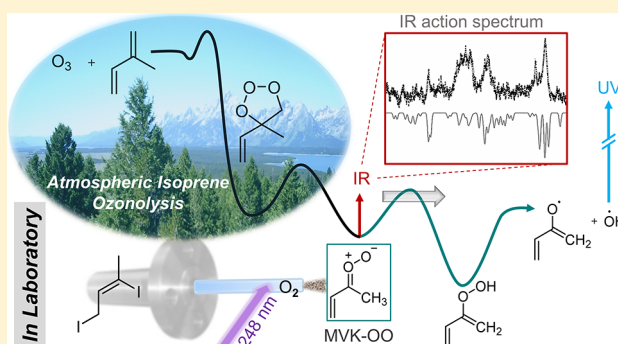
Victoria P. Barber,[†] Shubhrangshu Pandit,[†] Amy M. Green,[†] Nisalak Trongsiwat,[†] Patrick J. Walsh,[†] Stephen J. Klippenstein,[‡] and Marsha I. Lester^{*,†}

[†]Department of Chemistry, University of Pennsylvania, Philadelphia, Pennsylvania 19104-6323, United States

[‡]Chemical Sciences and Engineering Division, Argonne National Laboratory, Argonne, Illinois 60439, United States

Supporting Information

ABSTRACT: The reaction of ozone with isoprene, one of the most abundant volatile organic compounds in the atmosphere, produces three distinct carbonyl oxide species (RR'COO) known as Criegee intermediates: formaldehyde oxide (CH₂OO), methyl vinyl ketone oxide (MVK-OO), and methacrolein oxide (MACR-OO). The nature of the substituents (R,R' = H, CH₃, CH=CH₂) and conformations of the Criegee intermediates control their subsequent chemistry in the atmosphere. In particular, unimolecular decay of MVK-OO is predicted to be the major source of hydroxyl radicals (OH) in isoprene ozonolysis. This study reports the initial laboratory synthesis and direct detection of MVK-OO through reaction of a photolytically generated, resonance-stabilized monoiodoalkene radical with O₂. MVK-OO is characterized utilizing infrared (IR) action spectroscopy, in which IR activation of MVK-OO with two quanta of CH stretch at ca. 6000 cm⁻¹ is coupled with ultraviolet detection of the resultant OH products. MVK-OO is identified by comparison of the experimentally observed IR spectral features with theoretically predicted IR absorption spectra. For *syn*-MVK-OO, the rate of appearance of OH products agrees with the unimolecular decay rate predicted using statistical theory with tunneling. This validates the hydrogen atom transfer mechanism and computed transition-state barrier (18.0 kcal mol⁻¹) leading to OH products. Theoretical calculations reveal an additional roaming pathway between the separating radical fragments, which results in other products. Master equation modeling yields a thermal unimolecular decay rate for *syn*-MVK-OO of 33 s⁻¹ (298 K, 1 atm). For *anti*-MVK-OO, theoretical exploration of several unimolecular decay pathways predicts that isomerization to dioxole is the most likely initial step to products.



1. INTRODUCTION

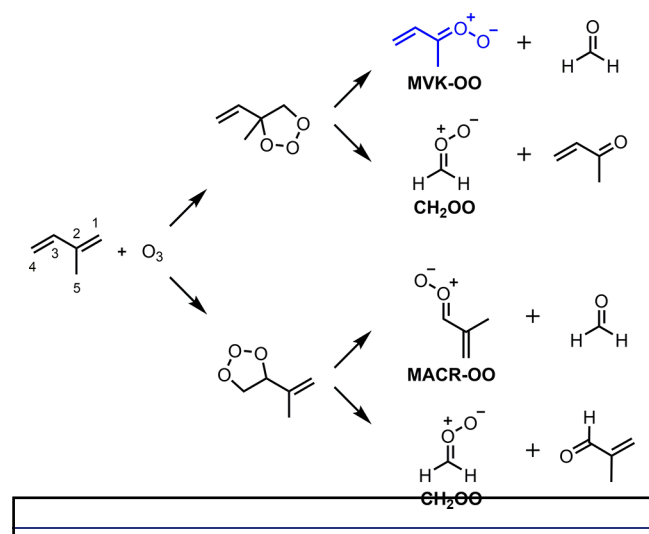
Isoprene (2-methyl-1,3-butadiene) is the most abundant volatile organic compound (VOC) in the Earth's troposphere after methane, with global emissions estimated at ca. 500 Tg/year.¹ In the atmosphere, the predominant removal pathways for isoprene (and other alkenes) are by reaction with the hydroxyl radical (OH), ozone (O₃), and the nitrate radical (NO₃; nighttime only).^{2–4} Globally, ozonolysis removes ca. 10% of isoprene⁵ and is an important pathway to OH radicals during daylight and nighttime conditions.⁶ The OH radical is the most important oxidant in the lower atmosphere and is sometimes referred to as “the atmosphere's detergent”.⁷ The OH yield from isoprene ozonolysis, however, is not well determined and may be pressure dependent.⁸ In earlier works, experimentally measured OH yields ranged from as low as ca. 20% to as high as ca. 70%, depending on the method used for OH detection.^{8–13} Recent measurements indicate an overall OH yield from isoprene ozonolysis of ca. 25%.^{5,14,15}

Alkene ozonolysis proceeds via highly energized carbonyl oxide species, termed Criegee intermediates, which represent a critical branching point controlling the products formed from this important class of reactions. The alkene ozonolysis reaction (Scheme 1) begins by cycloaddition of O₃ across a C=C double bond to form a primary ozonide (POZ).⁷ Isoprene has two distinct double bonds and can therefore produce two different POZs. Due to the asymmetry of each double bond, subsequent decomposition of each POZ can produce two Criegee intermediates and their corresponding carbonyl coproducts.^{5,9,16,17} Ozonolysis at the C₍₁₎=C₍₂₎ bond results in CH₂OO or methyl vinyl ketone oxide ((CH₂=CH)(CH₃)COO, MVK-OO)¹⁸ with their corresponding coproducts, methyl vinyl ketone ((CH₂=CH)(CH₃)CO, MVK) or formaldehyde (CH₂O), respectively. Ozonolysis at the C₍₃₎=C₍₄₎ bond results in either CH₂OO or methacrolein

Received: June 7, 2018

Published: August 3, 2018

Scheme 1. Criegee Intermediates and Co-products Formed in Ozonolysis of Isoprene



oxide ((CH₂=C(CH₃))CHOO, MACR-OO) with their corresponding coproducts, methacrolein ((CH₂=C(CH₃))-CHO, MACR) or formaldehyde, respectively. Combined experimental and theoretical evidence indicates an overall branching for isoprene ozonolysis of ca. 58% CH₂OO, ca. 23% MVK-OO and ca. 19% MACR-OO.^{5,19} This work focuses on MVK-OO, which is predicted to be the more abundant four-carbon unsaturated Criegee intermediate and the major source of OH radicals from atmospheric isoprene ozonolysis.⁵ MVK-OO is expected to differ substantially from previously investigated Criegee intermediates because of its extended π conjugation across the vinyl and carbonyl oxide functional groups.²⁰ MVK-OO is predicted to exhibit four conformers, as shown in Figure 1. Here, *syn* and *anti* refer to the orientation of

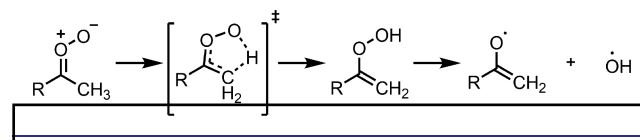
	<i>trans</i>	<i>cis</i>
<i>syn</i>	 0.00	 1.76
<i>anti</i>	 2.57	 3.05

Figure 1. Optimized structures and zero-point-corrected energies (kcal mol⁻¹) computed for the four conformers of the methyl vinyl ketone oxide (MVK-OO) Criegee intermediate. Geometries are optimized at the B2PLYP-D3/cc-pVTZ level of theory. Energies are calculated at the ANL0-B2F level of theory (see Table S2).

the methyl group with respect to the terminal oxygen of the carbonyl oxide group, while *cis* and *trans* refer to the orientation of the C=C and C=O bonds with respect to one another. The relative stabilities of the four conformers of MVK-OO differ by only ca. 3 kcal mol⁻¹, yet significant barriers restrict interconversion between them, as discussed below.¹⁶

In general, the atmospheric fate of the RR'COO Criegee intermediates is highly dependent on the conformation and nature of its substituents (R, R').²¹ In the atmosphere, Criegee intermediates can undergo prompt or thermal unimolecular decay to OH radicals and other products.^{7,22–25} Alternatively, collisionally stabilized Criegee intermediates can undergo bimolecular reaction with other atmospheric species, including water vapor and SO₂,^{26–32} which may result in aerosol formation and impact climate.³³ For *syn*-alkyl-substituted Criegee intermediates, such as *syn*-CH₃CHOO, (CH₃)₂COO, and the *syn* conformers of MVK-OO, unimolecular decay to OH is predicted to be the dominant atmospheric loss process.^{24,34–36} This reaction proceeds via a 1,4 H-atom transfer mechanism, whereby a *syn*-alkyl α -H-atom transfers to the terminal oxygen of the carbonyl oxide group via a 5-membered ring transition state (TS) to produce a vinyl hydroperoxide (VHP) species, which subsequently decays to generate OH, as shown in Scheme 2.^{23,37–39} Criegee

Scheme 2. Unimolecular Decay of *syn*-Alkyl-Substituted Criegee Intermediates to OH Radical

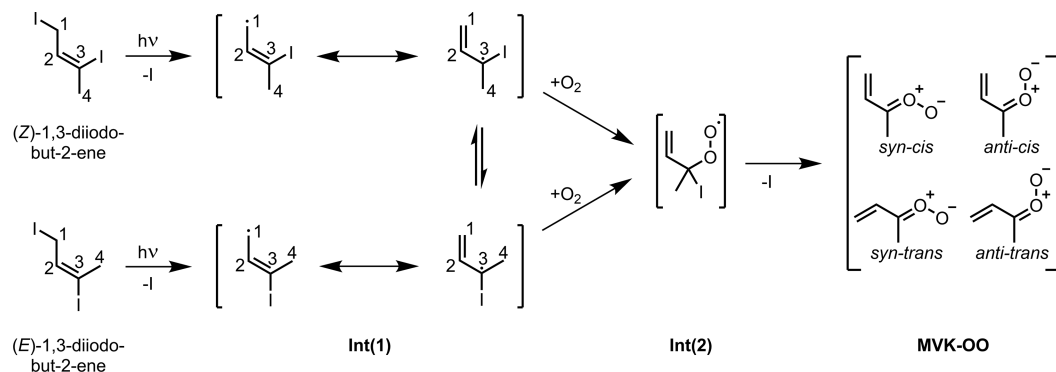


intermediates lacking a *syn*-alkyl α -H-atom, such as CH₂OO, *anti*-CH₃CHOO, *anti* conformers of MVK-OO (which have a more strongly bound vinylic α -H-atom), and MACR-OO (which has no α -H-atom) may decay unimolecularly via alternative pathways, but these are not anticipated to result in significant OH production.^{16,17,21,40,41} In particular, Criegee intermediates with a vinyl substituent in the *syn* position, such as *anti*-MVK-OO or *syn*-MACR-OO, are predicted to undergo an electrocyclic ring-closing reaction via a low barrier to form a 5-membered ring structure (cyc-CH₂OOC(CH₃)CH, dioxole).^{5,16,21} As a result, the *syn* conformers of MVK-OO are predicted to be the major source of OH radicals from isoprene ozonolysis.⁵

For Criegee intermediates with only an H-atom substituent in the *syn* position, such as CH₂OO or *anti*-CH₃CHOO, reactions with the water monomer and dimer are predicted to be the most important removal pathways in the atmosphere.^{28,30,31} However, for MVK-OO, reactions with water and water dimer are theoretically predicted to be very slow for all four conformers.^{42–45} Indeed, experimentally, there is no evidence for reaction between water vapor and MVK-OO during isoprene ozonolysis.⁵

In 2012, a new alternative synthetic route enabled direct experimental measurements of various small, prototypical Criegee intermediates.^{46,47} In this method, a *gem*-diiodoalkane precursor is photolyzed to produce a monoiodoalkyl radical, which subsequently reacts with O₂ to produce the Criegee intermediate. This class of reactions has proven useful for the production of a variety of Criegee intermediates including

Scheme 3. Alternate Synthetic Route to MVK-OO



CH₂OO,^{47,48} CH₃CHOO,^{46,49,50} (CH₃)₂COO,^{51,52} and CH₃CH₂CHOO.⁵² The four-carbon MVK-OO and MACR-OO Criegee intermediates generated in isoprene ozonolysis, which are arguably the most atmospherically relevant, have not been synthesized via this same method, because their corresponding *gem*-diiodo precursors are extremely reactive and cannot be prepared and purified. As a result, there has been no direct detection of MVK-OO prior to this report.

Recently, this group has studied several small prototypical Criegee intermediates, including *syn*-CH₃CHOO,³⁹ (CH₃)₂COO,³⁸ and *syn*-CH₃CH₂CHOO,⁵³ using infrared (IR) action spectroscopy with detection of OH radical products under collision-free conditions. IR activation of Criegee intermediates with two quanta of CH stretch (2ν_{CH}) accesses energies in the vicinity of the TS barrier to the 1,4 H-atom transfer reaction, and provides sufficient energy for the Criegee intermediates to surmount or tunnel through this barrier en route to OH products. This laboratory has also carried out rate measurements for unimolecular decay of the Criegee intermediates using IR activation with time-resolved detection of the resultant OH radical products.^{36,53} The experimentally determined OH appearance rates were found to be in excellent agreement with complementary statistical Rice–Ramsperger–Kassel–Marcus (RRKM) calculations utilizing high-level theoretical evaluation of the TS barrier height and incorporating quantum mechanical tunneling.

We anticipate that the *syn*-MVK-OO conformers will undergo a similar alkyl H-atom transfer mechanism to form OH radical products. As a result, we employ the sensitive and selective IR action spectroscopy technique to study the unimolecular decay of MVK-OO to OH. Several groups have predicted theoretical barriers for this process for the *syn* conformers of MVK-OO. For *syn-trans*-MVK-OO, these predictions range from 17.5 to 18.8 kcal mol⁻¹ (6120 to 6575 cm⁻¹),^{6,16,21,44} depending on the level of theory used, while for *syn-cis*-MVK-OO, they range from 16.9 to 18.4 kcal mol⁻¹ (5910 to 6435 cm⁻¹).^{6,16,44} [Note that barrier, well depth, and other energy terms utilized herein refer to zero-point-energy (ZPE)-corrected values.] IR activation of MVK-OO in the CH stretch overtone region at ca. 6000 cm⁻¹ is therefore expected to provide sufficient energy to surmount or tunnel through the reaction barrier and lead to OH products.

In this Article, we present the first direct observation of the MVK-OO Criegee intermediate. We introduce a new synthetic method that is used to produce the MVK-OO Criegee intermediate. We report the IR action spectrum of MVK-OO in the CH stretch overtone region with detection of OH radical products, which provides an IR fingerprint for MVK-

OO and demonstrates that IR activation of MVK-OO leads to OH and other products. Additionally, we present experimental measurements of the energy-dependent unimolecular decay rates for MVK-OO to OH products. Finally, we report theoretical calculations of electronic structure, vibrational frequencies, unimolecular decay mechanisms, and microcanonical and thermal decay rates for MVK-OO.

2. METHODS

2.1. Synthesis. A novel synthetic route is used to generate the methyl vinyl ketone oxide (MVK-OO) Criegee intermediate starting from a (Z/E)-1,3-diiodobut-2-ene precursor as introduced in Scheme 3. The synthesis and characterization of the precursor are described in detail in the Supporting Information (SI, section S1.1 and Figures S1–S3). Photolysis of 1,3-diiodobut-2-ene at 248 nm results in preferential dissociation of the weaker allylic C₍₁₎–I bond, rather than the vinylic (sp²-hybridized) C₍₃₎–I bond, due to resonance stabilization of the resultant allylic monoiodoalkene radical product Int(1).⁵⁴

The unique aspect of the present approach is based on the two resonance structures of the allylic monoiodoalkene radical Int(1). Although the radical center is initially formed at the C₍₁₎ carbon, delocalization will lead to the preferred radical site on the C₍₃₎ carbon due to its higher degree of substitution.⁵⁴ Subsequent reaction with O₂ is barrierless at the more stable carbon C₍₃₎ radical site as explained below. Addition of O₂ is expected to transiently form an energized iodoalkene peroxy radical Int(2), which can readily rotate about the C–C and C–O bonds before dissociation of I-atom resulting in formation of the four conformers of MVK-OO. The O₂ reaction step is similar to that leading to other Criegee intermediates from their corresponding geminal diiodo precursors.^{47–49,52,55}

Our theoretical calculations (see SI section S1.2) examine the minimum energy pathway (MEP) for O₂ addition to Int(1) at the C₍₃₎ vs C₍₁₎ site. As shown in Figure S4, a barrierless MEP is found for O₂ addition at C₍₃₎, while a saddle point is identified along the MEP for C₍₁₎, the latter causing a rate-limiting bottleneck for O₂ addition. As a result, the barrierless O₂ addition to Int(1) at the C₍₃₎ site is strongly favored both energetically and kinetically over addition at C₍₁₎.

2.2. Experimental Methods. The production of Criegee intermediates in a pulsed jet expansion has been described previously.^{48,49,52} In the present study, the diiodoalkene precursor is heated (60 °C) in a pulsed valve (Parker General Valve Series 9) with a Peltier thermoelectric heating module (Laird Technologies, PC4). The temperature is monitored with a thermocouple (Cole-Parmer, Type K digital thermometer). Heating increases the vapor pressure of the precursor and substantially increases the MVK-OO signal. The precursor is seeded in a 10% O₂/Ar carrier gas (30 psig), and pulsed through a nozzle (1 mm orifice) into a quartz capillary tube reactor (ca. 25 mm length, 1 mm ID). The precursor is photolyzed along the length of the capillary using the cylindrically focused 248 nm output (25 mJ pulse⁻¹) of a KrF excimer laser, which induces C–I bond

dissociation. Subsequent reaction of the resonance-stabilized monoiodoalkene radical with O₂ forms the MVK-OO Criegee intermediate. MVK-OO is initially detected by photoionization using 10.5 eV (118 nm) vacuum ultraviolet (VUV) radiation on the *m/z* = 86 mass channel of a time-of-flight mass spectrometer (TOF-MS, RM Jordan) as shown in Figure S6 and described in the SI (section S2; computed ionization energies for MVK-OO conformers are given in Table S1).

For IR pump–UV probe studies, MVK-OO is collisionally stabilized in the capillary and cooled in a free jet expansion to a rotational temperature of ~10 K.^{38,39} Approximately 1 cm downstream in the collision-free region, the gas mixture is intersected by counterpropagating and spatially overlapped IR pump and UV probe laser beams. The IR pump and UV probe lasers are focused to diameters of approximately 2 and 5 mm, respectively, in the interaction region. Tunable IR radiation is used to excite MVK-OO in the CH stretch overtone (2ν_{CH}) region, initiating unimolecular decay, and the UV laser then probes the resultant OH X²Π_{3/2} (*v* = 0) products via laser-induced fluorescence (LIF).

The tunable IR radiation (~20 mJ/pulse, 6 ns fwhm) used for spectroscopic experiments is the signal output of an optical parametric oscillator/amplifier (OPO/OPA, Laservision; 0.15 cm⁻¹ bandwidth), pumped by an injection-seeded Nd:YAG laser (Continuum Precision II 8000, 10 Hz). For rate measurements, the OPO/OPA is pumped with an unseeded Nd:YAG laser, yielding tunable IR radiation of ~30 mJ/pulse with a 0.9 cm⁻¹ bandwidth. The UV radiation (~4 mJ/pulse, 6 ns fwhm) is generated by frequency doubling the output of an Nd:YAG (Continuum 7020; 532 nm, 20 Hz) pumped dye laser (ND6000, Rhodamine 590 dye). The UV radiation is fixed on the OH A²Σ⁺–X²Π_{3/2} (1,0) Q₁(3,5) transition. Fluorescence is collected on the OH A²Σ⁺–X²Π_{3/2} (1,1) band with a gated photomultiplier tube (Electron Tubes 9813 QB). The output signal is preamplified and displayed on a digital storage oscilloscope (LeCroy WaveRunner 44Xi) interfaced with a computer for processing. An active background subtraction scheme (IR on–IR off) is used to remove background OH, which arises from the unimolecular decay of energized Criegee intermediates in the capillary and subsequent cooling in the free jet expansion.

Two types of experiments are performed: (1) The IR pump laser is scanned over the 2ν_{CH} energy region (5750–6260 cm⁻¹) at a fixed IR-UV time delay. Here, the time delay is set to 800 ns, which provides the optimal signal. The experimental method for acquiring IR action spectra of Criegee intermediates has been described previously.^{34,35,38,39} (2) The IR pump wavelength is fixed on a particular feature in the IR action spectrum, and the time delay between the IR pump and UV probe lasers is stepped in 20 ns increments to measure the time dependent appearance rate of OH radical products from IR-activated MVK-OO, as described previously for other Criegee intermediates.^{34–36,53}

2.3. Theoretical Methods. Complementary electronic structure calculations are carried out to characterize the energies of each MVK-OO conformer, barriers to conformational isomerization, as well as TS barriers and products of various unimolecular reactions. The present ab initio calculations were mostly performed with a slightly modified version of the ANL0-F12 approach described previously.⁵⁶ This approach (which we label as ANL0-B2F for ease of reference) is based on estimates of the complete basis set (CBS) CCSD(T) limit (via CCSD(T)-F12/CBS-F12(TZ-F12,QZ-F12)//B2PLYP-D3/cc-pVTZ calculations) together with a series of corrections as described in the SI (section S3). It differs from the ANL0-F12 approach by the replacement of the CCSD(T)/cc-pVTZ harmonic and B3LYP anharmonic rovibrational analyses with a B2PLYP-D3/cc-pVTZ analyses. We have also chosen to neglect the diagonal Born–Oppenheimer correction (DBOC) since it is often difficult to evaluate for TSs and rarely significant.

Our prior studies of related Criegee intermediates dissociations indicate that for rovibrational properties the B2PLYP-D3 approach is an effective alternative to CCSD(T) evaluations, at least for the initial H transfer from a Criegee intermediate to a vinyl hydroperoxide.³⁶ Furthermore, for a set of 147 molecules the CCSD(T)/CBS/B2PLYP-D3 energies are lower than the CCSD(T)/CBS//CCSD-

(T)/cc-pVTZ ones, indicating that the B2PLYP-D3 geometries are more accurate than CCSD(T)/cc-pVTZ ones. Meanwhile, for a set of 82 molecules the RMSD for B2PLYP-D3/cc-pVTZ and CCSD(T)/CBS ZPE values is only 0.11 kcal mol⁻¹. Thus, we expect the accuracy for the ANL0-B2F approach to be fairly similar to that for the ANL0-F12 approach, i.e. 2σ error bars of ~0.2–0.3 kcal mol⁻¹ for species with at most modest multireference character⁵⁶ (e.g., CCSDT(Q) corrections of 1.2 kcal mol⁻¹ or less). It is not clear how much the uncertainty is increased for species such as the Criegee intermediates of interest here where the multireference character is quite significant (perhaps a factor of 2 larger is a reasonable estimate; cf. Figure 14 of ref S6). It is perhaps worth noting though that our prior calculations with this methodology for various Criegee intermediate dissociations have yielded barrier heights that agree with experiment to much better than even the smaller uncertainties.^{36,53} The present ANL0-B2F stationary point energies are summarized in Table S2.

We are also interested in a number of aspects of the potential energy surface for which single reference methods are not appropriate. In particular, pathways involving stationary points with radical pairs or diradical configurations (see Tables S3–S5) require a multireference description. To explore the energetics of each of these pathways, we employ complete active space wave functions with both multireference second-order perturbation theory (CASPT2) and multireference singles and doubles configuration interaction (MRCISD+Q) including a fixed Davidson correction for the effect of higher order excitations. The uncertainties in the energies from these multireference calculations are likely much larger but still quite modest; i.e., 2σ error bars of 1 kcal mol⁻¹ or less (depending on the configuration). The electronic structure calculations described here were performed with Gaussian 09⁵⁷ (for the B2PLYP-D3 calculations), MOLPRO⁵⁸ (for the CASPT2, MRCISD+Q, and CCSD(T) evaluations), and CFOUR⁵⁹ (for most of the CCSDT(Q) calculations).

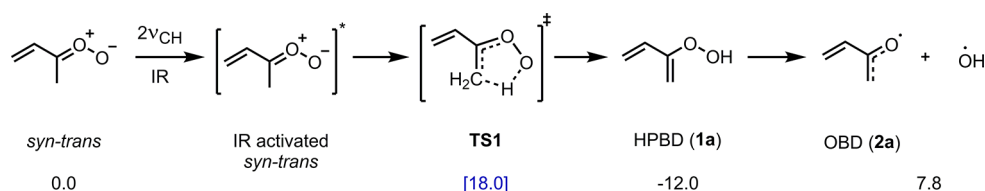
The IR spectra of MVK-OO in the 2ν_{CH} energy region is computed at the B2PLYP-D3/cc-pVTZ level of theory^{60–62} using vibrational second-order perturbation theory (VPT2) as implemented in Gaussian 09,⁵⁷ which has been previously demonstrated to provide highly accurate anharmonic vibrational frequencies for other Criegee intermediates.^{34,35,63} The results of these calculations are given in Table S6. For kinetic rate calculations, the rovibrational parameters (anharmonic fundamental vibrational frequencies, anharmonicity matrix and potential energy surfaces for methyl and vinyl torsional motion) of the reactants and TSs are also calculated at the same B2PLYP-D3/cc-pVTZ level of theory. Calculated anharmonic fundamental vibrational frequencies are given in Table S7 for the reactants and Table S8 for the TS.

Statistical RRKM theory is utilized to compute the energy-dependent unimolecular decay rate *k*(*E*) of *syn*-MVK-OO. The microcanonical rate constant *k*(*E*) is given by⁶⁴

$$k(E) = \frac{\sigma_{\text{eff}}^{\ddagger} G^{\ddagger}(E - E_0)}{\sigma_{\text{eff}}^{\ddagger} h N(E)}$$

where *E*₀ is the TS barrier energy, *G*[‡](*E* – *E*₀) is the sum of vibrational states at the TS, *N*(*E*) is the density of vibrational states in *syn*-MVK-OO, and *h* is Planck's constant. The effective symmetry numbers σ_{eff} are 1 for the reactants with a plane of symmetry, and 1/2 for the TSs with no symmetry and two enantiomers. The RRKM calculations utilize the computed energies and rovibrational properties of *syn*-MVK-OO, the TS, and products. The sums and densities of states are evaluated using anharmonic vibrational frequencies. The methyl and vinyl torsional modes of the *syn*-MVK-OO reactants and the vinyl torsional mode of the TS are treated as one-dimensional hindered rotors, as described in the SI (section S5). Tunneling is included in the RRKM calculations using either a one-dimensional asymmetric Eckart model as implemented in MESS^{65,66} or semiclassical transition-state theory (SCTST)^{67–72} as implemented in Multiwell.^{73–75} Additional RRKM calculations are carried out for unimolecular decay of *anti*-MVK-OO via ring closure to dioxole as described in the SI (section S5).

Scheme 4. Pathway for Unimolecular Decay of IR-Activated *syn-trans*-MVK-OO^a to OH Radical Products with Zero-Point-Corrected Energies (kcal mol⁻¹)



^aThere is an analogous pathway for *syn-cis*-MVK-OO.

3. RESULTS

The present study focuses on the IR action spectroscopy of MVK-OO, and the ensuing unimolecular decay dynamics and OH radical production. The experimental IR action spectrum of MVK-OO with detection of OH products is obtained by scanning the IR pump laser in the CH stretch overtone ($2\nu_{\text{CH}}$) region at a fixed IR pump-UV probe time delay. In separate experiments, the IR-UV time delay is stepped to determine the rate of OH appearance following the vibrational activation of MVK-OO. In both types of experiments, the OH ($\nu = 0$, $J = 3.5$) products are detected by laser-induced fluorescence (LIF) on the OH $A^2\Sigma^+ - X^2\Pi_{3/2}$ (1,0) Q_1 (3,5) transition to obtain the best signal-to-background ratio; the OH signal intensity peaks at $J = 2.5$. Complementary theoretical calculations are carried out to predict the IR absorption spectra of the MVK-OO conformers (section 3.2) and energy-dependent unimolecular dissociation rates $k(E)$ from *syn*-MVK-OO conformers to OH products (section 3.3).

3.1. MVK-OO Conformers. The minimum energy structures and ZPE-corrected energies of the four conformers of MVK-OO are shown in Figure 1, and are in good agreement with previous theoretical predictions.^{6,16} The four MVK-OO conformers have similar energies with the highest energy *anti-cis* conformer predicted to lie only 3.1 kcal mol⁻¹ higher in energy than the lowest energy *syn-trans* conformer; all four conformers are expected to be produced via the new synthetic route. The zero-point corrected barriers to interconversion between the conformers are also evaluated and shown in Figure S7. The barriers to interconversion between the two *syn* conformers or the two *anti* conformers are predicted to be relatively low (<10 kcal mol⁻¹), while the barrier to interconversion between the *syn* and *anti* conformers is quite high (ca. 30 kcal mol⁻¹).

The computed reaction coordinate for the unimolecular decay of *syn*-MVK-OO conformers to OH products is shown in Scheme 4 and Figure 2. The reaction proceeds via a 1,4 alkyl H-atom transfer mechanism through a 5-membered ring TS to produce 2-hydroperoxybuta-1,3-diene ((CH₂=CH)(CH₂)-COOH, HPBD (1a)), followed by rapid homolysis of the O–O bond to produce OH and oxybutadiene ((CH₂=CH)(CH₂)CO, OBD (2a)) radicals. An expanded theoretical mapping of the HPBD decay pathway is given in section 4.1. The pathway from the lowest energy *syn-trans*-MVK-OO conformer (0 kcal mol⁻¹) takes place via a TS barrier of 18.0 kcal mol⁻¹, while the higher energy *syn-cis*-MVK-OO conformer (1.8 kcal mol⁻¹) is predicted to have a TS barrier at 19.2 kcal mol⁻¹. Due to the low barrier to isomerization between the *cis* and *trans* conformers, unimolecular decay of the *syn-cis* conformer will mostly proceed via the lower energy TS with an effective barrier of 16.2 kcal mol⁻¹. The incipient HPBD (1a) product is computed to be 12.0 kcal mol⁻¹ lower

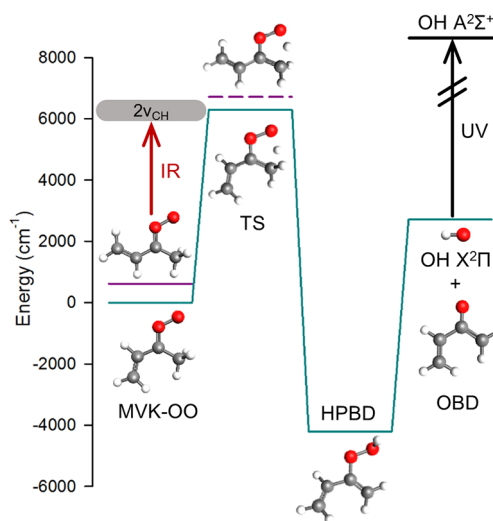


Figure 2. Computed reaction coordinate for unimolecular decay of *syn*-MVK-OO conformers to OH products. The reaction proceeds via a 1,4 alkyl H-atom transfer mechanism through a 5-membered ring-like transition state (TS) to produce 2-hydroperoxybuta-1,3-diene ((CH₂=CH)(CH₂)COOH, HPBD, 1a), followed by rapid homolysis of the O–O bond to produce OH and oxybutadiene ((CH₂=CH)(CH₂)CO, OBD, 2a) radicals. Stationary points along the reaction for the lowest energy *syn-trans*-MVK-OO conformer are shown (cyan line). Also shown are stationary points for the less stable *syn-cis*-MVK-OO conformer (solid purple line) and its higher energy TS (dashed purple line). The energy scale denotes ZPE-corrected energies for the stationary points. The IR pump laser (red arrow) excites *syn*-MVK-OO in the CH overtone region ($2\nu_{\text{CH}}$). The OH products are detected by UV probe laser (black arrow) induced fluorescence (LIF) on the OH A-X (1,0) transition.

in energy than *syn-trans*-MVK-OO. The resulting OBD (2a) and OH radical products are predicted to be 7.8 kcal mol⁻¹ higher in energy relative to *syn-trans*-MVK-OO.

3.2. IR Action Spectroscopy of MVK-OO. **3.2.1. Computed IR Absorption Spectrum.** Anharmonic vibrational frequencies and IR intensities in the CH stretch overtone region computed for the four conformers of MVK-OO are shown in Figure 3 and listed in Table S6. MVK-OO exhibits six high-frequency normal-mode vibrations (2900–3200 cm⁻¹) attributed to CH stretches. Four of these stretches involve in-plane motions (ν_1 – ν_4) and two involve out-of-plane motions: one in-phase (ν_5) and one out of phase (ν_{21}). Fundamental frequencies of these modes are given in Table S7. As a result, 21 IR transitions are expected for each conformer in the $2\nu_{\text{CH}}$ region (5750–6300 cm⁻¹): six CH stretch overtones (e.g., $2\nu_1$) and 15 CH stretch combinations comprised of one quantum each of two different CH stretches (e.g., $\nu_1 + \nu_2$), although some of these features are not predicted to have

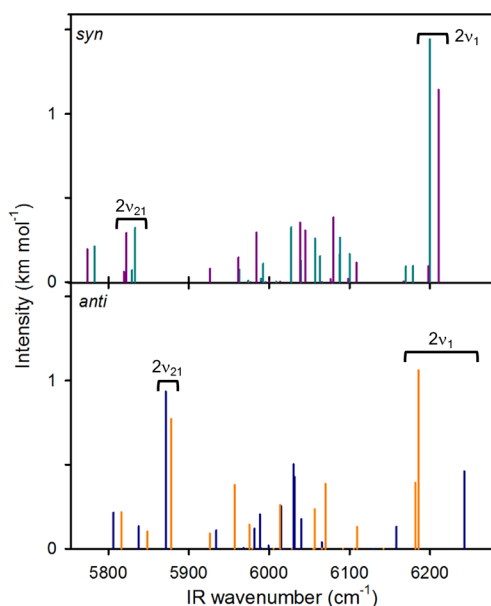


Figure 3. Computed anharmonic IR stick spectra for the four conformers of MVK-OO in the CH stretch overtone $2\nu_{\text{CH}}$ region at the B2PLYP-D3/cc-pVTZ level of theory. (Top panel) *syn-cis*-MVK-OO (purple) and *syn-trans*-MVK-OO (cyan). (Bottom panel) *anti-cis*-MVK-OO (blue) and *anti-trans*-MVK-OO (orange). Strong transitions attributed to the vinyl out-of-phase CH stretching mode ($2\nu_1$) and out-of-phase, out-of-plane, methyl CH stretch ($2\nu_{21}$) are labeled.

appreciable IR intensity. It should be noted that the intensities shown in these stick spectra reflect only the intrinsic calculated intensity of each IR transition and assume equal population of the conformers.

The highest energy transition predicted for each of the four MVK-OO conformers in the CH stretch overtone region arises from two quanta of the vinyl out-of-phase CH stretching mode ($2\nu_1$). For *syn*-MVK-OO, the $2\nu_1$ transitions of the *trans* and *cis* conformers lie within ca. 10 cm^{-1} of one another (6200.0 and 6210.4, respectively) and are the most intense transitions in this spectral region (with *cis* ca. 20% weaker than *trans*). In contrast, the $2\nu_1$ transitions of the *trans* and *cis* conformers of *anti*-MVK-OO are predicted to be separated by ca. 55 cm^{-1} , and are shifted to lower (*trans* at 6185.8 cm^{-1}) and higher (*cis* at 6242.9 cm^{-1}) frequency of the *syn*-MVK-OO transitions. The $2\nu_1$ transition of the *anti-trans* conformer is 2-fold stronger than that of *anti-cis*, and *anti-trans* has an overlapping $\nu_1 + \nu_2$ transition. Similar trends are predicted for the fundamental ν_1 transitions (Table S7).

Other prominent transitions in the computed IR spectra of *anti*-MVK-OO arise from two quanta excitation of the out-of-phase, out-of-plane, methyl CH stretch ($2\nu_{21}$) at 5871.3 and 5877.9 cm^{-1} for the *anti-cis* and *anti-trans* conformers, respectively. By contrast, the $2\nu_{21}$ transitions for the *syn-cis* and *syn-trans* conformers are predicted at significantly lower energy, 5822.3 and 5833.4 cm^{-1} , respectively, and are much weaker in intensity. Most other strong IR transitions for the four conformers are clustered between 5900 and 6150 cm^{-1} .

In the *syn* conformers, the methyl CH stretch overtone ($2\nu_{21}$) transitions are weaker in intensity and shifted to lower energy due to the intramolecular interaction between methyl group and the terminal oxygen of the carbonyl oxide group. In the *anti* conformers, the vinyl CH stretch overtone ($2\nu_1$) transitions are perturbed by the interaction of the vinyl group

with the terminal oxygen. These interactions give rise to the distinctive $2\nu_{21}$ and $2\nu_1$ transitions (Figure 3) predicted for the *syn* and *anti* conformers, respectively.

In general, the computed IR spectra for the two *syn* conformers are very similar to one another, as are the computed IR spectra for the two *anti* conformers. Due to the high barrier (ca. 30 kcal mol^{-1}) separating the *syn* and *anti* conformers (see Figure S7), the *syn* and *anti* conformers are chemically distinct species at the IR excitation energies explored in this work (5750–6300 cm^{-1} , 16.4–18.0 kcal mol^{-1}). However, the excitation energies are significantly higher than the predicted barriers separating the *cis* and *trans* conformers (ca. 10 kcal mol^{-1}), which may interconvert upon vibrational activation. Thus, in Figure 4, the computed IR

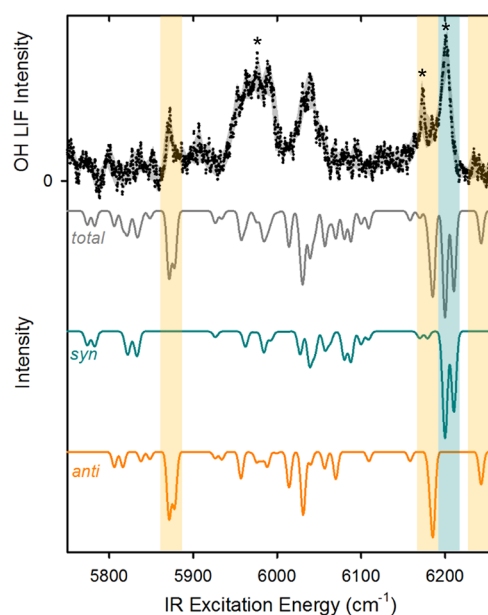


Figure 4. Experimental IR action spectrum of MVK-OO (black points) recorded in the CH stretch overtone $2\nu_{\text{CH}}$ region with UV laser-induced fluorescence (LIF) detection of OH at an IR-UV time delay of 800 ns. A smoothed fit (gray shaded area) that includes experimental uncertainty ($\pm 1.5\sigma$) is superimposed on the experimental data. The computed IR absorption spectra for the four conformers of MVK-OO (total, gray), the two *syn* conformers (*syn*, cyan), and the two *anti* conformers (*anti*, orange) are shown for comparison. The computed IR spectra are a convolution of the stick spectra (Figure 3) for the *syn* and *anti* conformers with a Gaussian profile (3 cm^{-1} width), representing the rotational band contour at ca. 10 K, and summed to give the total. The four conformers are assumed to be equally populated. The vertical shaded areas represent segments of the experimental spectrum attributed to the *syn* conformers (cyan) and the *anti* conformers (orange) of MVK-OO in comparison with theory. Asterisks indicate features at which experimental rate measurements are performed.

transitions for the two *syn* conformers are combined as are those for the two *anti* conformers, and then are convoluted with a Gaussian width of 3 cm^{-1} (fwhm). This width corresponds to the typical breadth of a simulated rotational band contour at 10 K as shown in Figure S8. In addition, the broadened spectra for the *syn* and *anti* conformers are summed together in Figure 4 assuming equal populations of the four conformers.

3.2.2. Experimental IR Action Spectrum. The experimental IR action spectrum of MVK-OO is obtained in the 5750–6260

cm^{-1} region with UV LIF detection of the resulting OH radical products at an IR-UV time delay of 800 ns, and is shown in Figure 4. Peak positions and relative intensities are given in Table S9. The IR-UV time delay is selected based on the experimentally determined OH appearance rates (section 3.3.1). The most intense feature in the spectrum appears at 6200.4 cm^{-1} , and is ascribed, based on its IR frequency and relative intensity, to the overlapping $2\nu_1$ transitions of *syn-cis*- and *syn-trans*-MVK-OO, as indicated by cyan vertical shading in Figure 4. Other relatively strong, sharp and isolated features in the experimental IR action spectrum agree remarkably well with predicted transitions for *anti*-MVK-OO conformers and are denoted by orange vertical shading in Figure 4. Specifically, the feature at 5869.6 cm^{-1} agrees well in IR frequency and relative intensity with the calculated overlapping $2\nu_{21}$ transitions of the *anti-trans* and *anti-cis* conformers. In addition, the feature at 6174.2 cm^{-1} agrees with the computed $2\nu_1$ and overlapping $\nu_1 + \nu_2$ transitions of *anti-trans*-MVK-OO. A much smaller feature at 6234.2 cm^{-1} is consistent with the predicted $2\nu_1$ transition of *anti-cis*-MVK-OO.

Additionally, the experimental IR action spectrum exhibits two relatively strong and quite broad features centered at ca. 6040 and 5975 cm^{-1} . The feature at 6040 cm^{-1} is consistent with a combination of overlapping transitions predicted theoretically for *syn* and *anti* conformers, most notably the $\nu_3 + \nu_4$ and $2\nu_3$ transitions of *anti-cis*-MVK-OO, and $2\nu_2$ and $2\nu_3$ transitions of *syn-cis*-MVK-OO. The feature at 5975 cm^{-1} is broader and stronger than suggested from the sum of the calculated transitions for *syn*- and *anti*-MVK-OO. The predicted spectrum, however, considers only two quanta vibrational changes and second-order couplings. This feature may arise from three or more quanta vibrational changes and/or higher order couplings between vibrational modes of MVK-OO, which will be explored in future work. Several weak features between 5750 and 5850 cm^{-1} are also observed, where both *syn* and *anti* conformers are predicted to have weak transitions. The overall shape of the experimentally observed IR action spectrum agrees qualitatively with the total spectrum computed for MVK-OO.

It is important to note that IR action spectroscopy differs from IR absorption spectroscopy in that the vibrationally excited molecule must generate OH products. For *syn* conformers, unimolecular decay to OH products proceeds via the 1,4 alkyl H-atom transfer pathway predicted for *syn*-MVK-OO (Figure 2 and Scheme 4) and other *syn*-alkyl-substituted Criegee intermediates. However, the mere observation of OH radical products following excitation of spectroscopic features attributed to *anti* conformers is surprising. The *anti* conformers of MVK-OO lack a *syn*-alkyl α -H-atom available for facile transfer, suggesting that OH is formed by a different mechanism. Possible pathways from *anti*-MVK-OO to OH products are considered in the Discussion (section 4.2). We also considered the possibility that other isomers of MVK-OO, e.g. HPBD and dioxole, could contribute to the IR action spectrum. However, these species have their own distinctive IR transitions (see Figure S9), are more stable (see Table S2) than MVK-OO, and will not undergo unimolecular decay to OH at the experimental excitation energies.

3.3. Unimolecular Decay of MVK-OO to OH Products.

3.3.1. Experimental Rate Measurements. The experimental rate of appearance of OH products is obtained from direct time-domain measurements following excitation of several

features in the IR action spectrum ascribed to MVK-OO by comparison with theory. The OH products appear on a hundreds of nanosecond time scale, and fall off on a greater than $1 \mu\text{s}$ time scale. The temporal profiles of the OH products are fit to a dual exponential function as in previous work.^{34–36,53,63} The exponential rise of OH products is attributed to the unimolecular decay of MVK-OO, while the slower exponential fall arises from purely experimental factors due to molecules moving out of the spatial region irradiated by the UV probe laser. A representative temporal profile of the OH products (Figure S10) along with details of the fitting procedure are given in the SI (section S4).

IR excitation of the strongest feature at 6200.4 cm^{-1} results in an exponential OH appearance rate of $(2.3 \pm 0.2) \times 10^6 \text{ s}^{-1}$ (with $\pm 1\sigma$ uncertainty), corresponding to a lifetime of $430 \pm 30 \text{ ns}$. This feature is attributed to the $2\nu_1$ transition of *syn*-MVK-OO. IR excitation at 6174.2 cm^{-1} yields a faster exponential rise rate of $(3.2 \pm 0.4) \times 10^6 \text{ s}^{-1}$, corresponding to a lifetime of $310 \pm 40 \text{ ns}$. This feature is ascribed to the $2\nu_1$ transition of *anti-trans*-MVK-OO based on theory, but lies on the shoulder of the stronger *syn*-MVK-OO feature at 6200.4 cm^{-1} . (A reliable rate measurement was not feasible for a weaker feature attributed to *anti*-MVK-OO at 5869.6 cm^{-1} .) Finally, IR excitation of the broad and unassigned feature at 5975.4 cm^{-1} results in a slower OH appearance rate of $(1.4 \pm 0.3) \times 10^6 \text{ s}^{-1}$, corresponding to a lifetime of $710 \pm 150 \text{ ns}$. The experimental OH rise and fall rates are summarized in Table S10; the OH appearance rates are also plotted in Figure 5.

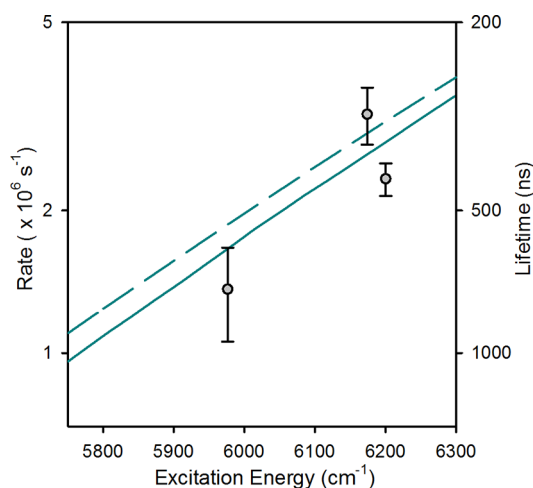


Figure 5. Experimentally observed rates and corresponding lifetimes (semi-log scales) for unimolecular decay of IR-activated MVK-OO to OH products (gray points) with $\pm 1\sigma$ uncertainty from repeated measurements (Table S10). Statistical RRKM rates for *syn-trans*-MVK-OO (cyan) are shown for comparison using asymmetric Eckart (solid cyan line) and SCTST (dashed cyan line) tunneling models.

3.3.2. RRKM Calculations. Statistical RRKM theory is utilized to compute the energy-dependent unimolecular decay rates $k(E)$ for the lowest energy *syn-trans* conformer of MVK-OO (see section 3.1). Quantum mechanical tunneling is included using an asymmetric Eckart model or semi-classical transition state theory (SCTST), which incorporate anharmonic vibrational frequencies, given in Table S7 for the reactants and Table S8 for the TS. The computed RRKM rates are predicted to increase uniformly with excitation energy as

Table 1. Comparison of ZPE-Corrected Stationary Point Energies (kcal mol⁻¹)

species	label	CCSD(T)// B3LYP ^a	CBS-QB3 ^b	MCG3 ^c	CCSD(T)// M06-2X ^d	present work
Minima						
<i>syn-trans</i> -MVK-OO		0	0	0	0	0
<i>syn-cis</i> -MVK-OO		1.5	1.7			1.76
<i>anti-trans</i> -MVK-OO		2.5	2.9			2.57
<i>anti-cis</i> -MVK-OO		2.7	2.9			3.05
<i>trans</i> -HPBD	1b	-14.9	-14.7			-13.83
<i>cis</i> -HPBD	1a	-13.7	-12.9			-12.02
dioxole	11		-25.6			-24.28
<i>trans</i> -dioxirane	6a	-17.0	-17.1			-15.28
<i>cis</i> -dioxirane	6b	-18.2	-18.6			-16.77
diradical	12		-23.1			-18.1
Transition States						
<i>syn-trans</i> -MVK-OO to <i>cis</i> -HPBD		18.8	18.0	18.34	17.5	17.96
<i>syn-cis</i> -MVK-OO to <i>trans</i> -HPBD		19.9	19.1	18.64 ^e		19.19
<i>anti-trans</i> -MVK-OO to AHP		24.4	21.7 ^f		23.6 ^e	24.57
<i>anti-cis</i> -MVK-OO to dioxole			13.9		13.9 ^e	15.06
<i>anti-cis</i> -MVK-OO to <i>cis</i> -dioxirane		24.9	24.9			25.38
<i>cis</i> -dioxirane to <i>syn-cis</i> -MVK-OO		21.0	20.9		21.0	21.35
<i>anti-trans</i> -MVK-OO to <i>trans</i> -dioxirane		20.0	19.7		19.8 ^e	19.93
<i>trans</i> -dioxirane to <i>syn-trans</i> -MVK-OO		22.1	22.2			22.44
<i>syn-trans</i> to <i>anti-trans</i> MVK-OO			26.0			30.93
<i>syn-cis</i> to <i>anti-cis</i> MVK-OO			23.5			30.63
dioxole to diradical			-4.9			-2.5
diradical to β -dicarbonyl			-19.5			-18.7

^aRef 6. ^bRef 16. ^cRef 44. ^dRef 21. Note that this work does not distinguish between *cis* and *trans* conformers of MVK-OO; only *syn* and *anti* conformers are identified. ^eThe energies of TS barriers in ref 21 are added to the ground-state energies of the relevant reactant reported in this work. We therefore add the TS barrier reported in ref 21 to the energy for *syn-cis*-MVK-OO reported herein. ^fWe repeated the calculation for *anti-trans*-MVK-OO to AHP (3-hydroperoxybuta-1,2-diene) using the CBS-QB3 method and obtained a barrier of 24.2 kcal mol⁻¹, which is in much better accord with the present work.

shown in Figure 5 and listed in Table S11. The computed unimolecular decay rate for *syn-trans*-MVK-OO at 6200 cm⁻¹ of 2.79×10^6 s⁻¹ (Eckart) or 3.08×10^6 s⁻¹ (SCTST) agrees well with the experimentally measured rate for appearance of OH radical products following IR excitation of *syn*-MVK-OO ($2\nu_1$) of $(2.3 \pm 0.2) \times 10^6$ s⁻¹. The 6200 cm⁻¹ excitation energy lies slightly below the computed *syn-trans* TS barrier (6288.7 cm⁻¹) demonstrating the importance of tunneling in the generation of OH products. The agreement between experiment and theory validates the 1,4 H-atom transfer mechanism and TS barrier for unimolecular decay of *syn-trans*-MVK-OO to OH products. In addition, the agreement demonstrates that the *syn-trans* conformer of MVK-OO is the principal spectral carrier near the peak of the strong $2\nu_1$ feature in the IR action spectrum at 6200.4 cm⁻¹ with minimal contribution from the $2\nu_1$ transition of the *syn-cis* conformer, theoretically predicted at 6210 cm⁻¹, as explained below.

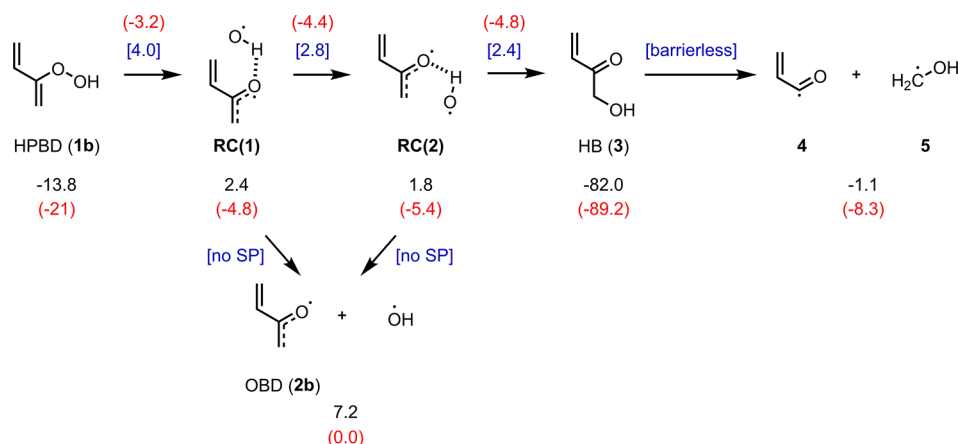
Due to the small barrier to isomerization between the *cis* and *trans* conformers of *syn*-MVK-OO, the two conformers are assumed to freely interconvert at energies near the TS barrier. As a result, the higher energy *syn-cis* conformer of MVK-OO (1.8 kcal mol⁻¹) will mostly proceed via the lower energy TS with an effective barrier of 16.2 kcal mol⁻¹. Furthermore, $2\nu_1$ excitation of the higher energy *syn-cis* conformer will access a higher vibrational state of *syn*-MVK-OO. These factors lead to the prediction of a ca. 4x faster RRKM rate for *syn-cis*-MVK-OO [9.99×10^6 s⁻¹ (Eckart) or 1.06×10^8 s⁻¹ (SCTST)] as shown in Figure S11 (Table S11)] than computed for *syn-trans*-MVK-OO at 6200 cm⁻¹. Indeed, the predicted RRKM

rates for *syn-cis*-MVK-OO are much faster than any of the experimental rates (Table S10). This suggests that the higher energy *syn-cis* conformer makes minimal contribution at 6200 cm⁻¹ due to less abundance of this conformer or the $2\nu_1$ transition of *syn-cis*-MVK-OO is shifted to higher wavenumber as predicted theoretically.

The experimental OH appearance rate at 6174.2 cm⁻¹ is more rapid than that observed for the higher energy feature at 6200.4 cm⁻¹ assigned to *syn-trans*-MVK-OO. This is not consistent with the general RRKM trend of slower rates at lower energies, e.g., as shown for *syn-trans*-MVK-OO (Figure 5). As discussed in section 3.2.2, the position of the observed feature at 6174.2 cm⁻¹ is consistent with the $2\nu_1$ transition predicted for *anti-trans*-MVK-OO. Nevertheless, the experimental rate at 6174.2 cm⁻¹, $(3.2 \pm 0.4) \times 10^6$ s⁻¹, does not differ sufficiently from the computed RRKM rate for *syn-trans*-MVK-OO at this energy [2.63×10^6 s⁻¹ (Eckart) or 2.92×10^6 s⁻¹ (SCTST)] to exclude the possibility of contribution to the rate from partial overlap of the adjacent *syn-trans*-MVK-OO feature at 6200.4 cm⁻¹. Despite the similarity in rate, the position of this and other spectroscopic features in Figure 4 (orange shading) are consistent with IR transitions predicted theoretically for *anti*-MVK-OO. In section 4.2, we consider plausible pathways from *anti* conformers of MVK-OO to OH products.

The computed unimolecular decay rate for *syn-trans*-MVK-OO at 5975 cm⁻¹ of 1.66×10^6 s⁻¹ (Eckart) or 1.87×10^6 s⁻¹ (SCTST) is also in good agreement with the experimentally measured OH appearance rate of $(1.4 \pm 0.3) \times 10^6$ s⁻¹ for IR-

Scheme 5. Unimolecular Decay Pathways for 2-Hydroperoxybut-1,3-diene (HPBD) with Zero-Point-Corrected Energies (kcal mol⁻¹) Relative to *syn-trans*-MVK-OO (Black/Blue) and OH + Oxybutadiene (OBD) Asymptote (Red)



activated MVK-OO at this energy. This suggests that there may be a contribution from *syn-trans*-MVK-OO to the broad feature in the IR action spectrum at 5975 cm⁻¹, although contributions from other conformers cannot be ruled out.

The energy-dependent unimolecular decay rates for MVK-OO to OH products may alter the intensities observed in the IR action spectrum at a fixed IR-UV time delay. For *syn-trans*-MVK-OO over the energy range (6260 to 5750 cm⁻¹) of the IR action spectrum, the OH appearance time will increase (280 to 1000 ns) toward lower energy. This will decrease the intensity observed at a fixed delay of 800 ns by a factor of 2 toward the lower energy extreme as shown in Figure S12, making it more difficult to observe the weaker transitions predicted at lower energy. Nevertheless, we expect to be able to detect vibrationally activated MVK-OO that decays to OH products on a microsecond or faster time scale (see SI, section S4).

4. DISCUSSION

Qualitative agreement between the overall shape of the experimental IR action spectrum and calculated IR absorption spectrum (Figure 4) demonstrate that MVK-OO is the spectral carrier and indicate the formation of OH radicals from MVK-OO. The OH production mechanism from *syn*-MVK-OO is described in the Results (section 3), illustrated in Scheme 4, and discussed further in section 4.1. Plausible mechanisms for OH production from *anti*-MVK-OO are presented in section 4.2, but are less certain and will require further investigation. The chemical names, chemical formulas, abbreviations, and labels used in the schemes and text are summarized in Table S13.

4.1. *syn*-MVK-OO. It is well accepted that OH production from Criegee intermediates with *syn*-alkyl substituents proceeds via 1,4 alkyl H-atom migration from the *syn*-alkyl group to the terminal O-atom.^{23,37–39} *syn*-MVK-OO is predicted to follow this same mechanism (Figure 2 and Scheme 4). The high-level calculation of the TS barrier in this work agrees within 1 kcal mol⁻¹ of the previously predicted barriers for this process (see Table 1). In addition, the computed RRKM rate with tunneling for unimolecular decay of *syn-trans*-MVK-OO is in quantitative agreement with the experimentally observed rate of OH production near the peak of the strong feature at 6200.4 cm⁻¹. This confirms that the IR spectral feature arises primarily from *syn-trans*-MVK-OO and

validates the TS barrier for the 1,4 alkyl H-atom transfer mechanism.

The unimolecular decay of *syn-trans*-MVK-OO (430 ± 30 ns) is significantly slower than previously observed for *syn*-CH₃CHOO (6.7 ± 0.2 ns at 5709 cm⁻¹), (CH₃)₂COO (18.5 ± 1.0 ns at 5971 cm⁻¹), and *syn*-CH₃CH₂CHOO (39.2 ± 2.6 ns at 5961 cm⁻¹) upon 2ν_{CH} excitation.^{36,53} The slower unimolecular decay for *syn-trans*-MVK-OO is primarily due to its higher TS barrier (18.0 kcal mol⁻¹) compared to *syn*-CH₃CHOO (17.05 kcal mol⁻¹), (CH₃)₂COO (16.16 kcal mol⁻¹), and *syn*-CH₃CH₂CHOO (16.46 kcal mol⁻¹),^{36,53} and larger density of states in the 2ν_{CH} region. For *syn-trans*-MVK-OO and previously studied *syn*-alkyl-substituted Criegee intermediates, H-atom tunneling significantly enhances the unimolecular decay rate and allows for OH production at energies much below the TS barrier.^{34–36,53,63}

Thus far, we have considered the rate-limiting 1,4 H-atom transfer pathway from *syn*-MVK-OO to HPBD (*cis*-HPBD, 1a), followed by a simple barrierless O–O bond dissociation to form OH + OBD (*cis*-OBD, 2a) products (see Scheme 4). However, further theoretical investigation using multireference methods reveals that dissociation of HPBD (1a) is not a simple, barrierless bond cleavage reaction, but rather the potential energy surface for this process is fairly complex and may lead to additional products as shown in Scheme 5. Note that in Scheme 5 and the discussion that follows in section 4.1, we provide energies relative to the separated OH + OBD (2b) products. This scheme is analogous to that recently suggested by Kuwata et al. for thermal decay of *syn*-CH₃CHOO and (CH₃)₂COO.⁷⁶ For simplicity, we display the reaction pathway from the lowest energy conformer of HPBD (*trans*-HPBD, 1b). [The *cis*-HPBD (1a) conformer is also accessible and will readily isomerize to *trans*-HPBD (1b).]

The unimolecular reaction pathway of HPBD (1b) begins with O–O bond elongation, passes over a small submerged saddle point (SP) at −3.2 kcal mol⁻¹, and leads to intermediate well RC(1) where OH + OBD (2b) are weakly interacting in the long-range region of the potential. Further elongation of the O–O bond continues smoothly (no SP) to OH + OBD (2b) products. Within the shallow well RC(1) (−4.8 kcal mol⁻¹), the H-side of the OH radical is in a strong hydrogen-bonding interaction with the O-site of OBD. These features along the minimum energy dissociation coordinate of HPBD

are consistent with previous theoretical studies of the reaction coordinate for *syn*-CH₃CHOO to OH radical products.^{77,78}

Alternatively, a roaming-induced unimolecular decay process may occur that involves the isomerization of the complex (RC(1)). In particular, the OH radical may roam in a relatively flat potential region from one side of the resonance stabilized OBD (2b) moiety to the other side to form another distinct weakly interacting hydrogen-bonded complex (RC(2)), in which the O-side of the OH radical is pointing toward the CH₂ group of the OBD (2b) fragment. Notably, the roaming SP (−4.4 kcal mol^{−1}) for this OH reorientation process (RC(1) ↔ RC(2)) lies considerably below the asymptotic energy of OH + OBD (2b). The second complex (RC(2)) may also undergo a barrierless (no SP) dissociation to OH + OBD (2b) products. An alternative roaming-induced isomerization reaction may occur from RC(2) by addition of the OH fragment to the CH₂ group of the OBD fragment to yield 1-hydroxybut-3-en-2-one (HB, 3) in a deep well (−89.2 kcal mol^{−1}). Under the collision free conditions of the present experiments, HB (3) formed via roaming would likely dissociate via CC bond fission to different radical products (4 + 5) that lie lower in energy (ca. 8.3 kcal mol^{−1}) than OO fission to OH + OBD (2b) products. Although not explored here, the pathway from HB (3) to products (4 + 5) may include a sequence of submerged SPs (denoted “barrierless” in Scheme 5). Under thermalized conditions, the roaming path may result predominantly in collisional stabilization of HB (3) in its deep well. Such a roaming induced isomerization pathway provides an explanation for the observation of hydroxy acetone in recent experiments involving thermalized (CH₃)₂COO.^{76,79} Thus, the roaming pathway from HPBD (1b) to HB (3) could potentially reduce the OH yield from IR-activated *syn*-MVK-OO.

The MEP for the roaming mechanism from HPBD (1b) to HB (3) is shown in Figure 6 using coordinates that reflect the distance and the angular orientation of OH relative to OBD (2b). The saddle points (SP) along the roaming pathway lie at least 4 kcal mol^{−1} lower in energy than the OH + OBD (2b) product asymptote. As a result, the roaming dynamics (i.e., the reorientation of OH between RC(1) and RC(2)) and the roaming mediated isomerization from RC(2) to HB (3) become accessible at a lower energy than OO bond fission. Thus, one might expect roaming to be a significant component of the dynamics under atmospheric conditions, which could alter the overall OH yield and the products formed from atmospheric isoprene ozonolysis.

4.2. anti-MVK-OO. Some features observed in the experimental IR action spectrum in the CH stretch overtone (2ν_{CH}) region are consistent with theoretically predicted IR transitions of *anti*-MVK-OO. In this section, we explore several unimolecular reaction routes theoretically to ascertain their viability as a source of OH from *anti* conformers of MVK-OO. In general, energies shown in the schemes are relative to the lowest energy *syn-trans* conformer of MVK-OO. Note that the *anti-trans* and *anti-cis* conformers lie 2.6 and 3.1 kcal mol^{−1} higher in energy, respectively, resulting in lower effective barriers for unimolecular reactions of *anti* conformers. An IR excitation energy of 5750–6260 cm^{−1} (16.4–17.9 kcal mol^{−1}) is utilized in the present experiments, which is much greater than the isomerization barrier between the two *anti*-MVK-OO conformers (ca. 8 kcal mol^{−1}). As a result, the same reaction pathways should be relevant for both *anti-cis* and *anti-trans* conformers.

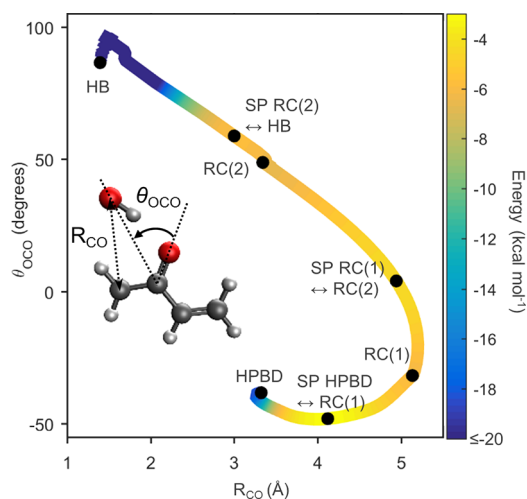
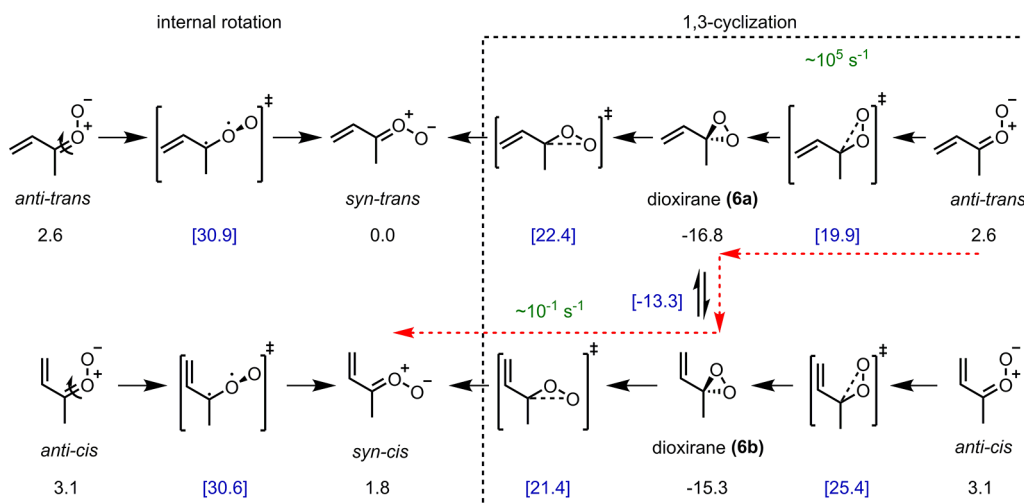
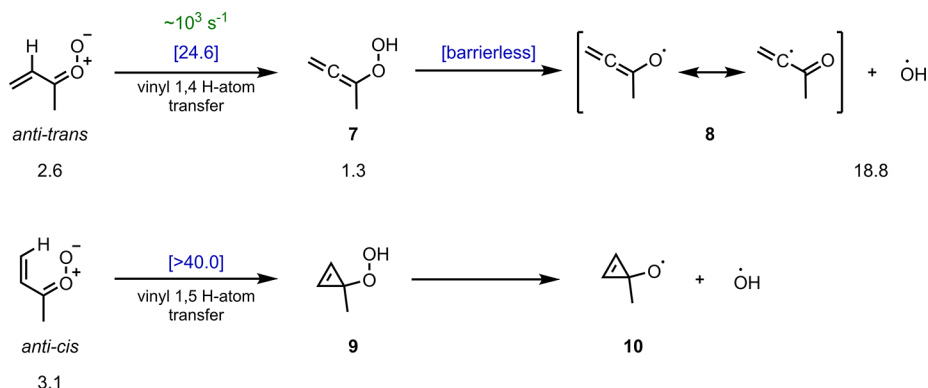
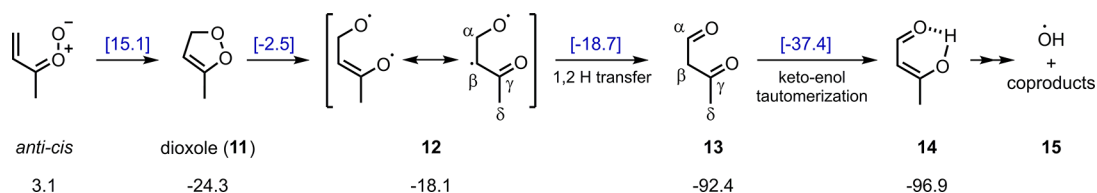


Figure 6. Minimum energy path for the roaming mechanism from *trans*-2-hydroperoxybuta-1,3-diene (*trans*-HPBD, 1b) to hydroxybutenone (HB, 3) is displayed as a function of two coordinates, CO bond distance (R_{CO}) and OCO angle (θ_{OCO}), as shown on the inset structure. The calculations are performed using the CASPT2(6e,6o)/cc-pVTZ method/basis. The color gradient represents the calculated energy (kcal mol^{−1}) with zero taken to be the separated OH and *trans*-oxybutadiene (*trans*-OBD, 2b) products. Points include roaming complexes RC(1) and RC(2) and saddle points (SP) along the pathway from HPBD to HB.

4.2.1. anti-to-syn Conformational Isomerization. Two different *anti*-to-*syn* isomerization pathways for MVK-OO are shown in Scheme 6. The first involves internal rotation about the C=O bond, as predicted previously.^{16,21} We have explored this isomerization pathway using a multireference description due to the diradical configurations of the TS. The lowest barrier to internal rotation is predicted to be 30.6 kcal mol^{−1} between the *anti-cis* and *syn-cis* conformers. Our calculated barriers are ca. 5–9 kcal mol^{−1} higher than those predicted by Kuwata et al.¹⁶ Most importantly, the predicted barriers are >10 kcal mol^{−1} greater than the excitation energies used in this experiment, indicating that this isomerization process cannot be a feasible pathway to OH radical products. We have also considered a second multistep *anti* to *syn* isomerization pathway in our calculations: ring closure to a dioxirane (6a) intermediate, followed by ring opening to *syn*-MVK-OO, as shown by the red arrows (*anti-trans*-MVK-OO to 6a to 6b to *syn-cis*-MVK-OO) within the dashed box in Scheme 6. The minimum energy route along this isomerization pathway involves surmounting a relatively high barrier of 21.4 kcal mol^{−1} for the isomerization from 6b to *syn-cis*-MVK-OO. At the excitation energies in this study, this rate-limiting step is expected to be very slow (ca. 10^{−1} s^{−1}). Therefore, isomerization from *anti*- to *syn*-MVK-OO and subsequent unimolecular decay is unlikely to be the mechanism by which OH is produced from *anti*-MVK-OO.

4.2.2. Vinyl H-Atom Transfer. Alternatively, an H-atom transfer from the vinyl substituent of *anti*-MVK-OO could produce a chemically excited hydroperoxide species (3-hydroperoxybuta-1,2-diene, AHP, 7) and lead to OH radical products. As indicated in Scheme 7 and Table 1,^{16,44} 1,4 vinyl H-atom transfer is feasible for *anti-trans*-MVK-OO, while 1,5 vinyl H-atom transfer is viable for *anti-cis*-MVK-OO. These reactions involve H-atom transfer, and may occur by tunneling at energies significantly below the TS barrier. In this work, we

Scheme 6. Two Different Isomerization Pathways from *anti*-MVK-OO to *syn*-MVK-OO with Zero-Point-Corrected Energies (kcal mol⁻¹)Scheme 7. Vinyl Hydrogen Atom Transfer Mechanisms from *anti*-MVK-OO to OH Radical Products with Zero-Point-Corrected Energies (kcal mol⁻¹)Scheme 8. Mechanism^a from *anti*-MVK-OO to OH Products via Dioxole Intermediate with Zero-Point-Corrected Energies (kcal mol⁻¹)

^aOH production from enol compound 14 likely involves a series of unimolecular rearrangements and is not well understood.

employ higher level theoretical calculations and predict a barrier of 24.6 kcal mol⁻¹ for *anti*-*trans*-MVK-OO. This barrier is ca. 7 kcal mol⁻¹ higher than that for *syn*-MVK-OO conformers (see Scheme 4), which can be understood by the loss of extended conjugation and the higher ring strain in the nonplanar TS geometry. At the excitation energies in this experiment, RRKM rate calculations with tunneling for vinyl 1,4 H-atom transfer indicate that the OH appearance rate would be extremely slow (ca. 10³ s⁻¹). Vereecken et al. previously reported a very high barrier of >40 kcal mol⁻¹ for 1,5 vinyl H-atom transfer in *anti*-*cis*-MVK-OO, and thus we have not explored this pathway.²¹ Therefore, the present calculations indicate that a vinyl H-atom transfer mechanism is

unlikely to be a significant source of OH products from *anti*-MVK-OO conformers.

4.2.3. Dioxole Pathways. We consider a third general decay pathway for *anti*-MVK-OO that starts with an electrocyclic ring closing of the *anti*-*cis* conformer to dioxole (11) and could lead to OH products as shown in Scheme 8. The transition states for the rearrangement from 11 to 12, 12 to 13, and then 13 to 14 are associated with diradical configurations. As a result, these TS energy calculations employ a multireference description. Our calculated effective barrier of 12.0 kcal mol⁻¹ for this isomerization process of *anti*-*cis*-MVK-OO is in reasonably good agreement with the 11.0 kcal mol⁻¹ barrier predicted by Kuwata et al.¹⁶ and the 11.9 kcal mol⁻¹ barrier predicted by Vereecken et al.²¹ The *anti*-*cis*-MVK-OO to

dioxole (11) pathway is predicted to have a significantly lower barrier than any other removal pathway for *anti* conformers considered in this or other works. Unimolecular decay rates from *anti*-MVK-OO to dioxole (11) are computed using RRKM theory as detailed in the SI and shown in Figure S13. This dioxole (11) formation is predicted to be rapid (ca. 10^8 s $^{-1}$) and thus, the dominant removal pathway for vibrationally activated *anti*-MVK-OO. Although there is no direct experimental evidence for isomerization of MVK-OO to dioxole (11), recent theoretical work by Kuwata et al. predicts that the dioxole (11) yield from MVK-OO could be as high as 36–42%.¹⁶ Thus, several possible pathways from dioxole (11) to OH radical products are explored theoretically in our high-level electronic structure calculations.

As shown in Scheme 8, the *anti*-*cis*-MVK-OO to dioxole (11) reaction is exothermic by 27.4 kcal mol $^{-1}$. Thus, the dioxole product (11) will be formed with a large amount of internal energy and can undergo further unimolecular processes. Kuwata et al. showed that dioxole (11) may decay via the homolytic O–O bond fission to form a diradical (12).¹⁶ Our calculation of the effective barrier from dioxole (11) to this diradical (12) is 21.8 kcal mol $^{-1}$, indicating that the ring-opening process from 11 to 12 will be facile. Next, the ring-opened diradical (12) can rearrange to a number of closed-shell dicarbonyl molecules as previously predicted by Kuwata et al.¹⁶

One possible rearrangement of the diradical (12) could lead to a β -dicarbonyl compound (3-oxobutanal, 13) through an intramolecular 1,2 H-atom transfer from C $_{(\alpha)}$ to C $_{(\beta)}$. This H-atom migration step leading to the β -dicarbonyl (13) product is highly exothermic (ca. -70 kcal mol $^{-1}$). As a result, numerous unimolecular rearrangements and dissociation pathways from the chemically activated β -dicarbonyl (13) will be energetically accessible under collision free conditions. Barrierless fission of the C $_{(\alpha)}$ –C $_{(\beta)}$ or C $_{(\beta)}$ –C $_{(\gamma)}$ bond can lead to various bimolecular products, but is not expected to generate OH products. Our preliminary rate calculations estimate these CC bond fission reactions to be very fast and likely the dominant *anti*-MVK-OO removal path.

We have also considered several possible rearrangement pathways starting from chemically activated β -dicarbonyl (13) that can lead to OH products. Previous theoretical work on similar diketone compounds (e.g., acetylacetone, CH $_3$ C(O)–CH $_2$ C(O)CH $_3$, and malonaldehyde, HC(O)CH $_2$ C(O)H) indicates that an isolated dicarbonyl compound with sufficient internal energy (ca. 100 kcal mol $^{-1}$) could tautomerize via an intramolecular H-atom transfer to an enol form over a barrier of ca. 60 kcal mol $^{-1}$.^{80,81} The resulting enol compounds are predicted to be more stable than the dicarbonyl tautomers due to the extended π -conjugation and intramolecular hydrogen bonding. There are many such energetically feasible rearrangement processes for chemically activated β -dicarbonyl (13) to various enol compounds, where the barriers along the reaction pathway would be readily surmounted.

Here, we consider a representative keto–enol tautomerization pathway from the β -dicarbonyl (13) to an enol (14) over an effective TS barrier of ca. 55 kcal mol $^{-1}$. The enol (14) will be formed with sufficient internal energy to undergo unimolecular decay and release the OH product in a single step process. Alternatively, the enol (14) could undergo multistep isomerization to other stable molecules with a OH group, which then readily dissociate to OH and a coproduct (15). The lowest energy coproduct (15) is predicted to be 1-

oxobut-2-enyl with three resonance structures. Our high-level electronic structure calculations predict all the stationary points following dioxole (11) to be downhill relative to *anti*-MVK-OO and thus energetically accessible. A theoretical treatment of unimolecular rates and OH yields is still needed, and will be the subject of future work.

Alternatively, it is possible that OH is formed via a UV-assisted photodissociation pathway. A UV light driven pathway to OH from enol compounds, including 14, has some precedence in the literature. For the enol form of acetylacetone (β -diketone), Messaadia et al. found a strong π -to- π^* transition centered at 260 nm, which extended to ca. 310 nm.⁸² In a different experiment, Yoon et al. observed OH products following excitation of the enol acetylacetone tautomer to the (π, π^*) state.^{83,84} In our experiment, 289 nm radiation is used for OH A-X (1,0) Q $_1$ (3.5) LIF detection. Hence, a UV light driven OH production pathway from the enol tautomer (14) cannot be ruled out. In this scenario, two sequential single-photon processes might lead to OH production. The first photon would pump the enol molecules to the electronic excited state and trigger the OH dissociation. A second UV photon would then probe the nascent OH X $^2\Pi_{3/2}$ ($\nu = 0$, $J = 3.5$) products within the 6 ns UV laser pulse (ca. 4 mJ pulse $^{-1}$). In this UV assisted pathway, formation of the enol compounds would likely be the rate-limiting step.

Finally, it is possible that the reaction occurs via a different mechanism that has not yet been considered. At this point, we can only speculate on the mechanism(s) leading from *anti* conformers of MVK-OO to OH products. We anticipate that selective deuteration of MVK-OO in future experiments, which are analogous to a previous study of partially deuterated *syn*-CD $_3$ CHOO,^{63,85} will provide further insight on the mechanistic pathway(s) leading to OH and/or OD products.

4.3. Thermal Decay of MVK-OO. Master equation modeling has been utilized to extend the microcanonical rates $k(E)$ to thermal rates $k(T)$ for unimolecular decay from *syn*-MVK-OO to HPBD and from *anti*-MVK-OO to dioxole under atmospheric conditions, as described previously for other Criegee intermediates.^{34–36,53} At 1 atm, master equation calculations suggest that the thermal rates for *syn* and *anti* MVK-OO are within 1% and 10% of the high pressure limit, respectively. The resultant thermal rates are displayed as an Arrhenius plot (semilog plot of $k(T)$ vs 1000/ T) in Figure 7.

For the unimolecular decay of *syn*-MVK-OO, the thermal rate at 298 K is predicted to be 33 s $^{-1}$. This is in very good accord with a thermal decay rate previously computed for *syn*-MVK-OO of 50 s $^{-1}$ by Vereecken et al.²¹ The *syn*-MVK-OO thermal rate is significantly slower than the thermal unimolecular decay rates computed for *syn*-CH $_3$ CHOO (166 s $^{-1}$),³⁵ (CH $_3$) $_2$ COO (276 s $^{-1}$),³⁴ and *syn*-CH $_3$ CH $_2$ CHOO (279 s $^{-1}$),^{53,86} as a result of the higher TS barrier associated with 1,4 H-atom transfer from *syn*-MVK-OO to HPBD.²⁰ The thermal decay rate for *syn*-MVK-OO is also slower than typically assumed rates (100–200 s $^{-1}$) for thermal loss of stabilized Criegee intermediates in atmospheric models.^{87,88} In the 200 to 350 K range, the thermal rate constant (high-pressure limit) is well represented by the modified Arrhenius expression $k(T) = (2.46 \times 10^{-76})T^{29.09} \exp(3545/T)$ s $^{-1}$. The curvature of the Arrhenius plot for *syn*-MVK-OO is indicative of the importance of tunneling in the thermal unimolecular decay process. Although the thermal rate signifies the unimolecular loss rate of *syn*-MVK-OO under atmospheric conditions, it may not equal the rate of OH production due to

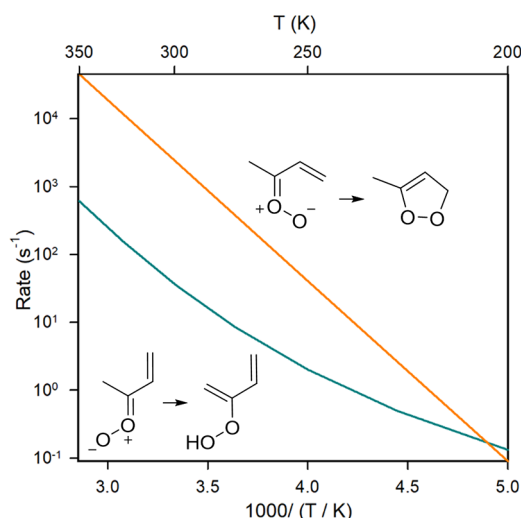


Figure 7. Arrhenius plot of the thermal decay rates $k(T)$ predicted for *syn*-MVK-OO to 2-hydroperoxybuta-1,3-diene (HPBD, cyan) and *anti*-MVK-OO to dioxole (orange). The curvature in the temperature-dependent thermal rates for *syn*-MVK-OO (cyan) originates from tunneling. Rates are computed using master equation modeling in the high pressure limit, and are plotted as a function of inverse temperature from 200 to 350 K.

the possibility of stabilization of HPBD and the likely contribution of the roaming pathway leading to HB products.

While the mechanism from *anti*-MVK-OO to OH is not well understood, the most important unimolecular loss process of *anti*-MVK-OO is predicted to be the electrocyclic reaction to dioxole. We calculate a relatively fast thermal unimolecular reaction rate to dioxole of 2140 s^{-1} , due to the low TS barrier for this process. This reaction does not involve tunneling and, as a result, the thermal rate can be represented by a simple Arrhenius expression, $k(T) = (1.94 \times 10^{12}) \exp(-6150/T) \text{ s}^{-1}$.

Unimolecular decay is expected to be the predominant removal pathway for both *syn*- and *anti*-MVK-OO under thermal conditions in the atmosphere. Much slower effective rates are predicted for bimolecular reaction of MVK-OO with water and water dimer under atmospheric conditions (e.g., 70% RH).^{42–44} However, the bimolecular rates for MVK-OO with trace atmospheric species, including SO_2 and NO_x , are not known and are important targets for future research.

5. CONCLUSIONS

This Article presents the first direct observation of the MVK-OO Criegee intermediate, which is the primary source of OH radicals in isoprene ozonolysis. MVK-OO is characterized by IR action spectroscopy in the CH stretch overtone region ($5700\text{--}6300 \text{ cm}^{-1}$) with detection of OH products. Spectral features in the IR action spectrum are in accord with calculated IR transitions of MVK-OO. Additionally, energy-dependent OH appearance rates from MVK-OO are measured and compared with theoretical predictions.

The unimolecular decay of *syn*-MVK-OO to OH products proceeds via a 1,4 H-atom transfer to HPBD followed by O–O bond cleavage to OH + OBD radical products. The experimentally measured OH appearance rate from vibrationally activated *syn*-MVK-OO at 6200 cm^{-1} agrees with the predicted RRKM rate including tunneling. This corroborates *syn*-MVK-OO as a spectral carrier, confirms the H-atom

transfer mechanism as the rate-determining step, and validates the calculated TS barrier ($18.0 \text{ kcal mol}^{-1}$). In addition, a roaming pathway is predicted to occur with the separating OH + OBD fragments reorienting at long range, leading to 1-hydroxybut-3-en-2-one (HB) or other products, and potentially reducing the OH yield.

The production of OH radicals from *anti*-MVK-OO is unexpected: previous work has predicted that *anti*-MVK-OO should be at most a minor source of OH.^{5,16,21} The mechanism of OH production from *anti*-MVK-OO is not well understood. Several possible pathways for OH production from *anti*-MVK-OO are investigated theoretically. *Anti*-to-*syn* isomerization pathways via internal rotation or 1,3 cyclization as well as vinyl H-atom transfer pathways are predicted to have barriers that are too high to facilitate unimolecular decay of *anti*-MVK-OO to OH under the present experimental conditions. Instead, *anti*-MVK-OO is expected to rapidly isomerize to the dioxole intermediate in a highly exothermic process. The internally excited dioxole can then undergo various unimolecular processes, such as O–O bond fission followed by rearrangement to a β -dicarbonyl and keto–enol tautomerization. However, only some dioxole decay pathways are predicted to yield OH products. Further theoretical work is needed to understand the mechanism for OH production from *anti*-MVK-OO. Additionally, planned experiments utilizing selective deuteration of MVK-OO will help to elucidate the mechanism from *anti*-MVK-OO to OH products.

Under atmospheric conditions, the thermal rate for unimolecular decay of *syn*-MVK-OO is predicted to be considerably slower (33 s^{-1} at 298 K, 1 atm) than those for previously studied alkyl-substituted Criegee intermediates,^{38,39,53} primarily because of its $1\text{--}2 \text{ kcal mol}^{-1}$ higher barrier. This provides an increased time window for *syn*-MVK-OO to undergo bimolecular reactions with atmospheric species, although the rates for such processes have not been experimentally measured. In addition, the OH product asymptote for *syn*-MVK-OO is higher than those in previously studied systems, suggesting an increased probability for collisional stabilization of the HPBD intermediate compared to other vinyl hydroperoxides. The OH product asymptote also lies considerably above the saddle point for roaming, indicating an increased likelihood of forming and therefore collisionally stabilizing the HB product from the roaming pathway. These processes may reduce the OH yield from *syn*-MVK-OO in the atmosphere. Finally, the thermal decay rate for *anti*-MVK-OO (2140 s^{-1} at 298 K, 1 atm) is predicted to be significantly faster than that for *syn*-MVK-OO. Many unimolecular processes and products are possible after initial decay to a dioxole intermediate.

This is the first report of the four-carbon, unsaturated MVK-OO Criegee intermediate, which is formed during isoprene ozonolysis. The novel synthetic procedure presented here opens up the possibility for many future experimental studies of this highly atmospherically relevant species. These include further spectroscopic studies, investigation of unimolecular decay under thermal conditions, kinetic rate measurements of bimolecular reactions with atmospheric species, and identification of products and yields.

■ ASSOCIATED CONTENT

Supporting Information

The Supporting Information is available free of charge on the ACS Publications website at DOI: 10.1021/jacs.8b06010.

Additional material on synthesis of MVK-OO, photoionization of precursor and MVK-OO Criegee intermediate, photoionization of diiodobutene precursor and MVK-OO Criegee intermediate, details of electronic structure calculations, spectral and kinetic analyses, and details of rate calculations, including Schemes S1 and S2, Figures S1–S13, and Tables S1–S14 (PDF)

AUTHOR INFORMATION

Corresponding Author

*milester@sas.upenn.edu

ORCID

Patrick J. Walsh: 0000-0001-8392-4150

Stephen J. Klippenstein: 0000-0001-6297-9187

Marsha I. Lester: 0000-0003-2367-3497

Notes

The authors declare no competing financial interest.

ACKNOWLEDGMENTS

The experimental research was primarily supported through the National Science Foundation under grant CHE-1664572 (M.I.L.). Partial equipment support was provided by the University of Pennsylvania Research Foundation (M.I.L.). Theoretical research was supported by the U.S. Department of Energy, Office of Science, Office of Basic Energy Sciences, Division of Chemical Sciences, Geosciences, and Biosciences under Contract No. DE-AC02-06CH11357 (S.J.K.) with partial support under grant DE-FG02-87ER13792 (M.I.L.). P.J.W. is grateful to the NSF (CHE-1464744 and DMR-1628407) for support of the synthetic research. The authors thank William P. Dailey for helpful discussions. The authors gratefully acknowledge John Stanton for making available a parallel version of the CCSDT(Q) component of the CFour code and David Bross for installing that code on our local Linux cluster.

REFERENCES

- (1) Sindelarova, K.; Granier, C.; Bouarar, I.; Guenther, A.; Tilmes, S.; Stavrakou, T.; Müller, J. F.; Kuhn, U.; Stefani, P.; Knorr, W. *Atmos. Chem. Phys.* **2014**, *14*, 9317–9341.
- (2) Atkinson, R.; Arey, J. *Acc. Chem. Res.* **1998**, *31*, 574–583.
- (3) Atkinson, R.; Arey, J. *Chem. Rev.* **2003**, *103*, 4605–4638.
- (4) Atkinson, R.; Arey, J. *Atmos. Environ.* **2003**, *37*, 197–219.
- (5) Nguyen, T. B.; Tyndall, G. S.; Crounse, J. D.; Teng, A. P.; Bates, K. H.; Schwantes, R. H.; Coggon, M. M.; Zhang, L.; Feiner, P.; Miller, D. O.; Skog, K. M.; Rivera-Rios, J. C.; Dorris, M.; Olson, K. F.; Koss, A.; Wild, R. J.; Brown, S. S.; Goldstein, A. H.; de Gouw, J. A.; Brune, W. H.; Keutsch, F. N.; Seinfeld, J. H.; Wennberg, P. O. *Phys. Chem. Chem. Phys.* **2016**, *18*, 10241–10254.
- (6) Zhang, D.; Zhang, R. *J. Am. Chem. Soc.* **2002**, *124*, 2692–2703.
- (7) Johnson, D.; Marston, G. *Chem. Soc. Rev.* **2008**, *37*, 699–716.
- (8) Kroll, J. H.; Hanisco, T. F.; Donahue, N. M.; Demerjian, K. L.; Anderson, J. G. *Geophys. Res. Lett.* **2001**, *28*, 3863–3866.
- (9) Gutbrod, R.; Kraka, E.; Schindler, R. N.; Cremer, D. *J. Am. Chem. Soc.* **1997**, *119*, 7330–7342.
- (10) Paulson, S. E.; Chung, M.; Sen, A. D.; Orzechowska, G. *J. Geophys. Res.: Atmos.* **1998**, *103*, 25533–25539.
- (11) Atkinson, R.; Aschmann, S. M.; Arey, J.; Shorees, B. *J. Geophys. Res.* **1992**, *97*, 6065–6073.
- (12) Rickard, A. R.; Johnson, D.; McGill, C. D.; Marston, G. *J. Phys. Chem. A* **1999**, *103*, 7656–7664.
- (13) Paulson, S. E.; Flagan, R. C.; Seinfeld, J. H. *Int. J. Chem. Kinet.* **1992**, *24*, 103–125.
- (14) Malkin, T. L.; Goddard, A.; Heard, D. E.; Seakins, P. W. *Atmos. Chem. Phys.* **2010**, *10*, 1441–1459.
- (15) Ren, Y.; Gosselin, B.; Daele, V.; Mellouki, A. *Faraday Discuss.* **2017**, *200*, 289–311.
- (16) Kuwata, K. T.; Valin, L. C.; Converse, A. D. *J. Phys. Chem. A* **2005**, *109*, 10710–10725.
- (17) Kuwata, K. T.; Valin, L. C. *Chem. Phys. Lett.* **2008**, *451*, 186–191.
- (18) The abbreviation MVK-OO is adopted from Wennberg and co-workers (ref 5).
- (19) Aschmann, S. M.; Atkinson, R. *Environ. Sci. Technol.* **1994**, *28*, 1539–1542.
- (20) Yin, C.; Takahashi, K. *Phys. Chem. Chem. Phys.* **2017**, *19*, 12075–12084.
- (21) Vereecken, L.; Novelli, A.; Taraborrelli, D. *Phys. Chem. Chem. Phys.* **2017**, *19*, 31599–31612.
- (22) Kroll, J. H.; Sahay, S. R.; Anderson, J. G.; Demerjian, K. L.; Donahue, N. M. *J. Phys. Chem. A* **2001**, *105*, 4446–4457.
- (23) Donahue, N. M.; Drozd, G. T.; Epstein, S. A.; Presto, A. A.; Kroll, J. H. *Phys. Chem. Chem. Phys.* **2011**, *13*, 10848–10857.
- (24) Drozd, G. T.; Kurten, T.; Donahue, N. M.; Lester, M. I. *J. Phys. Chem. A* **2017**, *121*, 6036–6045.
- (25) Novelli, A.; Vereecken, L.; Lelieveld, J.; Harder, H. *Phys. Chem. Chem. Phys.* **2014**, *16*, 19941–19951.
- (26) Mauldin, R. L., III; Berndt, T.; Sipilä, M.; Paasonen, P.; Petäjä, T.; Kim, S.; Kurtén, T.; Stratmann, F.; Kerminen, V. M.; Kulmala, M. *Nature* **2012**, *488*, 193–196.
- (27) Hakala, J. P.; Donahue, N. M. *J. Phys. Chem. A* **2016**, *120*, 2173–2178.
- (28) Chao, W.; Hsieh, J.-T.; Chang, C.-H.; Lin, J. J.-M. *Science* **2015**, *347*, 751–754.
- (29) Huang, H.-L.; Chao, W.; Lin, J. J.-M. *Proc. Natl. Acad. Sci. U. S. A.* **2015**, *112*, 10857–10862.
- (30) Lin, L.-C.; Chang, H.-T.; Chang, C.-H.; Chao, W.; Smith, M. C.; Chang, C.-H.; Lin, J. J.-M.; Takahashi, K. *Phys. Chem. Chem. Phys.* **2016**, *18*, 4557–4568.
- (31) Lewis, T. R.; Blitz, M. A.; Heard, D. E.; Seakins, P. W. *Phys. Chem. Chem. Phys.* **2015**, *17*, 4859–4863.
- (32) Kroll, J. H.; Seinfeld, J. H. *Atmos. Environ.* **2008**, *42*, 3593–3624.
- (33) Mentel, T. F.; Springer, M.; Ehn, M.; Kleist, E.; Pullinen, I.; Kurtén, T.; Rissanen, M.; Wahner, A.; Wildt, J. *Atmos. Chem. Phys.* **2015**, *15*, 6745–6765.
- (34) Fang, Y.; Barber, V. P.; Klippenstein, S. J.; McCoy, A. B.; Lester, M. I. *J. Chem. Phys.* **2017**, *146*, 134307.
- (35) Fang, Y.; Liu, F.; Barber, V. P.; Klippenstein, S. J.; McCoy, A. B.; Lester, M. I. *J. Chem. Phys.* **2016**, *145*, 234308.
- (36) Fang, Y.; Liu, F.; Barber, V. P.; Klippenstein, S. J.; McCoy, A. B.; Lester, M. I. *J. Chem. Phys.* **2016**, *144*, 061102.
- (37) Vereecken, L.; Francisco, J. S. *Chem. Soc. Rev.* **2012**, *41*, 6259–6293.
- (38) Liu, F.; Beames, J. M.; Lester, M. I. *J. Chem. Phys.* **2014**, *141*, 234312.
- (39) Liu, F.; Beames, J. M.; Petit, A. S.; McCoy, A. B.; Lester, M. I. *Science* **2014**, *345*, 1596–1598.
- (40) Nguyen, T.-N.; Putikam, R.; Lin, M. C. *J. Chem. Phys.* **2015**, *142*, 124312.
- (41) Nguyen, T. L.; Lee, H.; Matthews, D. A.; McCarthy, M. C.; Stanton, J. F. *J. Phys. Chem. A* **2015**, *119*, 5524–5533.
- (42) Anglada, J. M.; Gonzalez, J.; Torrent-Sucarrat, M. *Phys. Chem. Chem. Phys.* **2011**, *13*, 13034–13045.
- (43) Anglada, J. M.; Sole, A. *Phys. Chem. Chem. Phys.* **2016**, *18*, 17698–17712.
- (44) Kuwata, K. T.; Hermes, M. R.; Carlson, M. J.; Zogg, C. K. *J. Phys. Chem. A* **2010**, *114*, 9192–9204.
- (45) Aplincourt, P.; Anglada, J. M. *J. Phys. Chem. A* **2003**, *107*, 5798–5811.

- (46) Taatjes, C. A.; Welz, O.; Eskola, A. J.; Savee, J. D.; Scheer, A. M.; Shallcross, D. E.; Rotavera, B.; Lee, E. P. F.; Dyke, J. M.; Mok, D. K. W.; Osborn, D. L.; Percival, C. J. *Science* **2013**, *340*, 177–180.
- (47) Welz, O.; Savee, J. D.; Osborn, D. L.; Vasu, S. S.; Percival, C. J.; Shallcross, D. E.; Taatjes, C. A. *Science* **2012**, *335*, 204–207.
- (48) Beames, J. M.; Liu, F.; Lu, L.; Lester, M. I. *J. Am. Chem. Soc.* **2012**, *134*, 20045–20048.
- (49) Beames, J. M.; Liu, F.; Lu, L.; Lester, M. I. *J. Chem. Phys.* **2013**, *138*, 244307.
- (50) Sheps, L.; Scully, A. M.; Au, K. *Phys. Chem. Chem. Phys.* **2014**, *16*, 26701–26706.
- (51) Chang, Y.-P.; Chang, C.-H.; Takahashi, K.; Lin, J. J.-M. *Chem. Phys. Lett.* **2016**, *653*, 155–160.
- (52) Liu, F.; Beames, J. M.; Green, A. M.; Lester, M. I. *J. Phys. Chem. A* **2014**, *118*, 2298–2306.
- (53) Fang, Y.; Liu, F.; Klippenstein, S. J.; Lester, M. I. *J. Chem. Phys.* **2016**, *145*, 044312.
- (54) Isaacs, N. *Physical Organic Chemistry*, 2nd ed.; Longman Scientific & Technical: Harlow, Essex, England, 1995.
- (55) Su, Y.-T.; Huang, Y.-H.; Witek, H. A.; Lee, Y.-P. *Science* **2013**, *340*, 174–176.
- (56) Klippenstein, S. J.; Harding, L. B.; Ruscic, B. *J. Phys. Chem. A* **2017**, *121*, 6580–6602.
- (57) Frisch, M. J.; Trucks, G. W.; Schlegel, H. B.; Scuseria, G. E.; Robb, M. A.; Cheeseman, J. R.; Scalmani, G.; Barone, V.; Mennucci, B.; Petersson, G. A.; Nakatsuji, H.; Caricato, M.; Li, X.; Hratchian, H. P.; Izmaylov, A. F.; Bloino, J.; Zheng, G.; Sonnenberg, J. L.; Hada, M.; Ehara, M.; Toyota, K.; Fukuda, R.; Hasegawa, J.; Ishida, M.; Nakajima, T.; Honda, Y.; Kitao, O.; Nakai, H.; Vreven, T.; Montgomery, J. A., Jr.; Peralta, J. E.; Ogliaro, F.; Bearpark, M.; Heyd, J. J.; Brothers, E.; Kudin, K. N.; Staroverov, V. N.; Kobayashi, R.; Normand, J.; Raghavachari, K.; Rendell, A.; Burant, J. C.; Iyengar, S. S.; Tomasi, J.; Cossi, M.; Rega, N.; Millam, J. M.; Klene, M.; Knox, J. E.; Cross, J. B.; Bakken, V.; Adamo, C.; Jaramillo, J.; Gomperts, R.; Stratmann, R. E.; Yazyev, O.; Austin, A. J.; Cammi, R.; Pomelli, C.; Ochterski, J. W.; Martin, R. L.; Morokuma, K.; Zakrzewski, V. G.; Voth, G. A.; Salvador, P.; Dannenberg, J. J.; Dapprich, S.; Daniels, A. D.; Farkas, Ö.; Foresman, J. B.; Ortiz, J. V.; Cioslowski, J.; Fox, D. J. *Gaussian 09*, Revision D.01; Gaussian, Inc.: Wallingford, CT, 2009.
- (58) Werner, H.-J.; Knowles, P. J.; Knizia, G.; Manby, F. R.; Schütz, M.; Celani, P.; Gyröffy, W.; Kats, D.; Korona, T.; Lindh, R.; Mitrushenkov, A.; Rauhut, G.; Shamasundar, K. R.; Adler, T. B.; Amos, R. D.; Bernhardsson, A.; Berning, A.; Cooper, D. L.; Deegan, M. J. O.; Dobbyn, A. J.; Eckert, F.; Goll, E.; Hampel, C.; Hesselmann, A.; Hetzer, G.; Hrenar, T.; Jansen, G.; Köppl, C.; Liu, Y.; Lloyd, A. W.; Mata, R. A.; May, A. J.; McNicholas, S. J.; Meyer, W.; Mura, M. E.; Nicklaß, A.; O'Neill, D. P.; Palmieri, P.; Peng, D.; Pflüger, K.; Pitzer, R.; Reiher, M.; Shiozaki, T.; Stoll, H.; Stone, A. J.; Tarroni, R.; Thorsteinsson, T.; Wang, M. *MOLPRO, a Package of ab initio Programs*, 2015; www.molpro.net.
- (59) Stanton, J. F.; Gauss, J.; Cheng, L.; Harding, M. E.; Matthews, D. A.; Szalay, P. G.; Auer, A. A.; Bartlett, R. J.; Benedikt, U.; Berger, C.; Bernholdt, D. E.; Bomble, Y. J.; Christiansen, O.; Engel, F.; Faber, R.; Heckert, M.; Heun, O.; Hilgenberg, M.; Huber, C.; Jagau, T.-C.; Jonsson, D.; Jusélius, J.; Kirsch, T.; Klein, K.; Lauderdale, W. J.; Lipparini, F.; Metzroth, T.; Mück, L. A.; O'Neill, D. P.; Price, D. R.; Prochnow, E.; Puzzarini, C.; Ruud, K.; Schiffrmann, F.; Schwalbach, W.; Simmons, C.; Stopkowitz, S.; Tajti, A.; Vázquez, J.; Wang, F.; Watts, J. D. *CFOUR, Coupled-Cluster techniques for Computational Chemistry, a Quantum-Chemical Program Package*, www.cfour.de.
- (60) Grimme, S.; Ehrlich, S.; Goerigk, L. *J. Comput. Chem.* **2011**, *32*, 1456–1465.
- (61) Goerigk, L.; Grimme, S. *J. Chem. Theory Comput.* **2011**, *7*, 291–309.
- (62) Kendall, R. A.; Dunning, T. H.; Harrison, R. J. *J. Chem. Phys.* **1992**, *96*, 6796–6806.
- (63) Green, A. M.; Barber, V. P.; Fang, Y.; Klippenstein, S. J.; Lester, M. I. *Proc. Natl. Acad. Sci. U. S. A.* **2017**, *114*, 12372–12377.
- (64) Baer, T.; Hase, W. L. *Unimolecular Reaction Dynamics Theory and Experiments*; Oxford University Press: New York, 1996.
- (65) Georgievskii, Y.; Klippenstein, S. J. *MESS.2016.3.23*; Argonne National Laboratory, 2016; <http://tcg.cse.anl.gov/papr/codes/mess.html>.
- (66) Georgievskii, Y.; Miller, J. A.; Burke, M. P.; Klippenstein, S. J. *J. Phys. Chem. A* **2013**, *117*, 12146–12154.
- (67) Miller, W. H. *J. Chem. Phys.* **1975**, *62*, 1899–1906.
- (68) Miller, W. H. *Faraday Discuss. Chem. Soc.* **1977**, *62*, 40–46.
- (69) Miller, W. H.; Hernandez, R.; Handy, N. C.; Jayatilaka, D.; Willetts, A. *Chem. Phys. Lett.* **1990**, *172*, 62–68.
- (70) Hernandez, R.; Miller, W. H. *Chem. Phys. Lett.* **1993**, *214*, 129–136.
- (71) Nguyen, T. L.; Stanton, J. F.; Barker, J. R. *Chem. Phys. Lett.* **2010**, *499*, 9–15.
- (72) Nguyen, T. L.; Stanton, J. F.; Barker, J. R. *J. Phys. Chem. A* **2011**, *115*, S118–S126.
- (73) Barker, J. R. *Int. J. Chem. Kinet.* **2001**, *33*, 232–245.
- (74) Barker, J. R.; Nguyen, T. L.; Stanton, J. F.; Aieta, C.; Ceotto, M.; Gabas, F.; Kumar, T. J. D.; Li, C. G. L.; Lohr, L. L.; Maranzana, A.; Ortiz, N. F.; Preses, J. M.; Simmie, J. M.; Sonk, J. A.; Stimac, P. J. *MultiWell-2017 Software Suite*; University of Michigan, Ann Arbor, 2017; <http://clasp-research.engin.umich.edu/multiwell/>.
- (75) Barker, J. R. *Int. J. Chem. Kinet.* **2009**, *41*, 748–763.
- (76) Kuwata, K. T.; Luu, L.; Weberg, A. B.; Huang, K.; Parsons, A. J.; Peebles, L. A.; Rackstraw, N. B.; Kim, M. J. *J. Phys. Chem. A* **2018**, *122*, 2485–2502.
- (77) Kidwell, N. M.; Li, H.; Wang, X.; Bowman, J. M.; Lester, M. I. *Nat. Chem.* **2016**, *8*, 509–514.
- (78) Kurtén, T.; Donahue, N. M. *J. Phys. Chem. A* **2012**, *116*, 6823–6830.
- (79) Taatjes, C. A.; Liu, F.; Rotavera, B.; Kumar, M.; Caravan, R.; Osborn, D. L.; Thompson, W. H.; Lester, M. I. *J. Phys. Chem. A* **2017**, *121*, 16–23.
- (80) Yamabe, S.; Tsuchida, N.; Miyajima, K. *J. Phys. Chem. A* **2004**, *108*, 2750–2757.
- (81) Alagona, G.; Ghio, C. *Int. J. Quantum Chem.* **2008**, *108*, 1840–1855.
- (82) Messaadia, L.; El Dib, G.; Ferhati, A.; Chakir, A. *Chem. Phys. Lett.* **2015**, *626*, 73–79.
- (83) Yoon, M.-C.; Choi, Y. S.; Kim, S. K. *Chem. Phys. Lett.* **1999**, *300*, 207–212.
- (84) Yoon, M.-C.; Choi, Y. S.; Kim, S. K. *J. Chem. Phys.* **1999**, *110*, 11850–11855.
- (85) Kroll, J. H.; Donahue, N. M.; Cee, V. J.; Demerjian, K. L.; Anderson, J. G. *J. Am. Chem. Soc.* **2002**, *124*, 8518–8519.
- (86) Lester, M. I.; Klippenstein, S. J. *Acc. Chem. Res.* **2018**, *51*, 978–985.
- (87) Percival, C. J.; Welz, O.; Eskola, A. J.; Savee, J. D.; Osborn, D. L.; Topping, D. O.; Lowe, D.; Utembe, S. R.; Bacak, A.; Mc Figgans, G.; Cooke, M. C.; Xiao, P.; Archibald, A. T.; Jenkin, M. E.; Derwent, R. G.; Riipinen, I.; Mok, D. W. K.; Lee, E. P. F.; Dyke, J. M.; Taatjes, C. A.; Shallcross, D. E. *Faraday Discuss.* **2013**, *165*, 45–73.
- (88) Taatjes, C. A.; Shallcross, D. E.; Percival, C. J. *J. Phys. Chem. Chem. Phys.* **2014**, *16*, 1704–1718.